Markovian Statistical Model of Cloud Optical Thickness. Part I: Theory and Examples

MIKHAIL D. ALEXANDROV,[a,b] ALEXANDER MARSHAK,[c] BRIAN CAIRNS,[b] AND ANDREW S. ACKERMAN[b]

[a] *Department of Applied Physics and Applied Mathematics, Columbia University, New York, New York*
[b] *NASA Goddard Institute for Space Studies, New York, New York*
[c] *NASA Goddard Space Flight Center, Greenbelt, Maryland*

(Manuscript received 29 May 2022, in final form 15 August 2022)

ABSTRACT: We present a generalization of the binary-value Markovian model previously used for statistical characterization of cloud masks to a continuous-value model describing 1D fields of cloud optical thickness (COT). This model has simple functional expressions and is specified by four parameters: the cloud fraction, the autocorrelation (scale) length, and the two parameters of the normalized probability density function of (nonzero) COT values (this PDF is assumed to have gamma-distribution form). Cloud masks derived from this model by separation between the values above and below some threshold in COT appear to have the same statistical properties as in binary-value model described in our previous publications. We demonstrate the ability of our model to generate examples of various cloud-field types by using it to statistically imitate actual cloud observations made by the Research Scanning Polarimeter (RSP) during two field experiments.

KEYWORDS: Clouds; Statistical techniques; Cloud parameterizations; Numerical analysis/modeling; Stochastic models

1. Introduction

This study follows the "Cellular Statistical Models of Broken Cloud Fields" series of papers (Alexandrov et al. 2010a,b, hereinafter CSM1 and CSM2, respectively; Alexandrov and Marshak 2017, 2019, hereinafter CSM3 and CSM4, respectively). In these series we developed statistical parameterization and modeling algorithms for cloud structure in binary-mixture framework. The approach adopted there is based on cloud-mask statistics of 1D or 2D broken cloud fields derived from observations [in the 2D case made along 1D linear transects (chords)]. Such observations consist of the lengths of cloudy and clear intervals in each transect. The cloud statistics in this approach are always finite, so it works equally well for cumulus and stratocumulus cloud fields with a smooth transition between these two types (which are symmetrical to each other under cloud–clear interchange). This is an advantage compared to, e.g., area-based characterization which yields infinite cloud areas in Sc cases and infinite clear areas in Cu cases. In CSM2 the analytical expressions derived in CSM1 were demonstrated to adequately describe the statistics of shallow, broken cloud fields generated using a realistic large-eddy simulation (LES) model. In CSM3 the results of CSM1 were interpreted in terms of the theory of Markov processes (e.g., Kulkarni 2011; Ibe 2013). This interpretation is based on the assumption that each 1D sample consisting of subsequent cloudy and clear segments is a realization of a binary Markov process, which can take only two (generally nonnumerical) values: occupied (cloudy, "•") or empty (clear, "○"). In CSM4 the binary Markov processes framework was used for quantitative evaluation of the effects of low resolution of idealized observations on the statistics of the retrieved cloud masks.

In the above described approach cloud mask statistics depend on the nominal threshold in continuous-value field [such as cloud optical thickness (COT)] separating "clear" from "cloudy," which is chosen rather subjectively by the investigator. In this study we want to overcome this subjectivity by turning our attention from Markovian cloud mask model to this of the underlaying continuous-value cloud fields themselves. The continuous-value fields used in this study are these of COT which can take values ranging from zero to (formally) infinity. They will be characterized in our model by four statistical parameters: the absolute (zero-threshold) cloud fraction, the autocorrelation (scale) length, and the two parameters of the normalized probability density function of nonzero COT values (this PDF is assumed to have gamma-distribution functional shape).

Our approach to COT modeling is substantially simpler than those developed in the past, in particular, compared to the following two types of stochastic models of cloud horizontal structure. The first is the bounded cascade model (Marshak et al. 1993, 1994; Cahalan 1994) which is a nonstationary two-parameter generalization of Meneveau and Sreenivasan's p-models for the intermittent dissipation rate field in turbulence (Meneveau and Sreenivasan 1987). The second class, suggested by Schertzer and Lovejoy (1987), consists of fractionally integrated cascade models where power-law filtering in Fourier space brings the spectral exponent to any prescribed value.

We will show that the binary Markovian model described in CSM3 can be derived from our continuous-value Markovian model by attribution of the COT values to binary classes using a selected cloud/clear separation threshold. The data points with values higher than this threshold are attributed to the class • (cloudy), while those with values lower than the threshold are attributed to the class ○ (clear). The corresponding binary statistics (cloud fraction, spatial scale, transition probabilities, etc.) can be derived from the continuous Markovian

Corresponding author: Mikhail D. Alexandrov, mda14@columbia.edu

DOI: 10.1175/JAS-D-22-0125.1

model by integration from zero to the threshold for ∘ and from the threshold to infinity for •.

Realizations of the continuous-value model are piecewise constant 1D functions, which, nevertheless, look quite realistic. We will demonstrate this by generating synthetic COT fields, which imitate those actually observed by the airborne Research Scanning Polarimeter (RSP) during two field campaigns. The examples will include various cloud-field types: Cu, Sc, and As.

2. Binary Markovian model of broken cloud field

The theoretical framework for Markovian parameterization of broken cloud field statistics was presented in CSM3. Here we outline the main points.

a. Cloud mask statistics

Cloud fields representing a binary Markovian model on the real line $\mathbb{R}$ are infinite 1D patterns of interchanging clear and cloudy intervals of finite lengths. The statistical distributions of lengths of these intervals appear to be exponential (Levermore et al. 1988; Pomraning 1989; CSM1) with the means $L_\bullet$ and $L_\circ$ of cloudy and clear intervals, respectively. The pair of numbers $(L_\bullet, L_\circ)$ provides complete parameterization of the model in the infinite space. This parameterization, however, is not unique and not the most convenient. An alternative set of two independent parameters can be chosen as (cf. Levermore et al. 1988; Pomraning 1989; CSM3)

$$\bar{c} = \frac{L_\bullet}{L_\bullet + L_\circ} \quad \text{and} \quad L_* = \frac{L_\bullet L_\circ}{L_\bullet + L_\circ}, \tag{1}$$

where $\bar{c}$ is the cloud fraction (CF) on $\mathbb{R}$ and L_* is the double of the harmonic mean of $L_\bullet$ and $L_\circ$:

$$\frac{1}{L_*} = \frac{1}{L_\bullet} + \frac{1}{L_\circ}. \tag{2}$$

The inverse of the relationship in Eq. (1) is

$$L_\bullet = \frac{L_*}{\bar{s}} \quad \text{and} \quad L_\circ = \frac{L_*}{\bar{c}}, \tag{3}$$

where $\bar{s} = 1 - \bar{c}$. The parameter L_* can be considered as a universal scale length of the cloud field. This parameter is also called "autocorrelation length" (cf. Levermore et al. 1988; Pomraning 1989) since it enters the exponent of the corresponding autocorrelation function (Morf 1998, 2011) (see also section 6 below). Note, however, that in order to define autocorrelation function, "•" and "∘" should be assigned with numerical values (e.g., 1 and 0).

In addition to infinite-length realizations of the binary Markovian model, the ensemble of finite-length samples extracted from these realizations was considered in CSM1. It was demonstrated in CSM2 that the same analysis is valid for finite 1D transects extracted from a 2D cloud field (in that case LES-simulated cloud masks). The sampling procedure is specified by the length L of the sample(s) and the probabilities of its initial point to be cloudy or clear. If the samples are chosen at random, their initial states are • with the probability $\bar{c}$ and ∘ with the probability $\bar{s}$.

b. Idealized observations

The image of the cloud field obtained by an idealized airborne or satellite sensor is the result of sampling with finite sample size L and finite resolution l. Multiple images with the same parameters constitute the observational dataset. A sequence of consecutive • points is considered a cloud, while a sequence of consecutive ∘ points is considered a gap. The mean observed lengths of such "clouds" and "gaps" $[L_\bullet^{(\mathrm{obs})}$ and $L_\circ^{(\mathrm{obs})}$, respectively] are then computed. The observed $\bar{c}^{(\mathrm{obs})}$ and $L_*^{(\mathrm{obs})}$ can be then derived according to Eq. (1).

While both finite sample size and resolution do not bias sampling estimates of $\bar{c}$ (which is simply the mean CF of the ensemble of samples), they introduce biases in the spatial cloud statistics, which should be corrected. The finite sample size results in cutting both actual clouds and gaps at sample edges, thus biases their mean length low. This effect was investigated in CSM1 resulting in the following recovery formula:

$$\frac{1}{L_i} = \frac{1}{L_i^{(\mathrm{obs})}} - \frac{1}{L}, \tag{4}$$

where $i =$ • or ∘; thus,

$$\frac{1}{L_*} = \frac{1}{L_*^{(\mathrm{obs})}} - \frac{2}{L}. \tag{5}$$

The final sampling resolution has the opposite effect: two clouds separated by a subpixel gap are observed as a larger single cloud. The same is true for two gaps separated by a subpixel cloud, both biasing high the estimate of L_*. This effect was in the focus of CSM4 where the following correction was introduced:

$$L_* = -l\left[\ln\left(1 - \frac{l}{L_*^{(\mathrm{obs})}}\right)\right]^{-1}, \tag{6}$$

which works well for sufficiently fine measurement resolution ($l < 5L_*$). Below both corrections will be used sequentially: first Eq. (5), and then Eq. (6). However, our inability to address both effects simultaneously may result in some small biases in estimation of L_*.

c. Markovian properties

As we already mentioned, realizations of a binary Markovian model are stochastic functions on real line $\mathbb{R}$ which can take only two values (states): "•" or "∘." The Markovian property of the model means that for any chosen initial point $x_0 \in \mathbb{R}$ the probabilities of the points $x > x_0$ to be in one of the two states depend only on the state of x_0 itself (and not on the states of the previous points $x < x_0$). These probabilities are combined into the transition probability matrix of the form

$$\mathbf{P} = \begin{pmatrix} P_{\bullet\bullet} & P_{\bullet\circ} \\ P_{\circ\bullet} & P_{\circ\circ} \end{pmatrix}, \tag{7}$$

where P_{ij} is the probability of transition from the state i at x_0 into the state j at $x > x_0$ (i and j can be either • or ∘). By definition of transition probabilities, each row of $\mathbf{P}$ sums to unity:

$$P_{\bullet\bullet} + P_{\bullet\circ} = 1 \quad \text{and} \quad P_{\circ\circ} + P_{\circ\bullet} = 1. \tag{8}$$

The description of the state of a point $x_0 \in \mathbb{R}$ can be generalized from being fixed (• or ∘) to stochastic: it is • with the probability u and ∘ with the complimentary probability $v = 1 - u$. In this case the state of x_0 can be characterized by the vector

$$\mathbf{u} = (u\ v), \tag{9}$$

and the transition from the state $\mathbf{u}$ at x_0 to the state $\mathbf{u}'$ at $x > x_0$ is the result of matrix multiplication:

$$\mathbf{u}' = \mathbf{u}\mathbf{P}, \tag{10}$$

or explicitly,

$$(u'\ v') = (u\ v)\begin{pmatrix} P_{\bullet\bullet} & P_{\bullet\circ} \\ P_{\circ\bullet} & P_{\circ\circ} \end{pmatrix}, \tag{11}$$

where

$$u' = uP_{\bullet\bullet} + vP_{\circ\bullet}, \quad v' = uP_{\bullet\circ} + vP_{\circ\circ}. \tag{12}$$

Equivalent description of point's state and transition was introduced in CSM3 (and extensively used in CSM4), replacing vector $\mathbf{u}$ with the "state matrix"

$$\mathbf{U} = \begin{pmatrix} u & v \\ u & v \end{pmatrix}, \tag{13}$$

which has the same structure as the transition matrix. In this formulation the state transition between two points is

$$\mathbf{U}' = \mathbf{U}\mathbf{P}. \tag{14}$$

The state of a point randomly selected from the ensemble is described by the vector

$$\mathbf{c} = (\bar{c}\ \bar{s}) \tag{15}$$

and is called "random state" in CSM3. It corresponds to the random-state matrix

$$\mathbf{C} = \begin{pmatrix} \bar{c} & \bar{s} \\ \bar{c} & \bar{s} \end{pmatrix}. \tag{16}$$

We assume the model to be spatially homogeneous, so the transition matrix depends only on the distance (lag) $L = x - x_0$, rather than on x and x_0 themselves: $\mathbf{P} = \mathbf{P}(L)$. We denote both sample length and transition lag by the same letter L since the formalism described in CSM3 provides a unified description of the cloud-field statistics in the sample and the probabilities of transition between its ends.

The transition matrices for two consequent intervals with lengths L_1 and L_2 obey the two group properties:

$$\mathbf{P}(L \to 0) = \mathbf{I}, \tag{17}$$

and

$$\mathbf{P}(L_1 + L_2) = \mathbf{P}(L_1)\mathbf{P}(L_2), \tag{18}$$

where $\mathbf{I}$ is the identity matrix. In the case of regular Markov process the random-state matrix Eq. (16) can be considered as the transition matrix in the limit $L \to \infty$ when correlation between the states at points x and $x + L$ is lost:

$$\mathbf{P}(L \to \infty) = \mathbf{C}. \tag{19}$$

The specific form of the transition matrix $\mathbf{P}$ was derived in CSM3 by integration of the "master matrix" over cloud fraction (see CSM3 for definitions and details), while it can be also obtained using other methods (see, e.g., Ibe 2013; Morf 1998; Kassianov 2003; Kassianov and Veron 2011; Kulkarni 2011), including directly from the constraints Eqs. (17)–(19) (see appendix A). The expression for $\mathbf{P}$ can be written in the following compact form:

$$\mathbf{P}(L) = w_L\mathbf{I} + (1 - w_L)\mathbf{C}, \tag{20}$$

where

$$w_L = e^{-L/L_*} = e^{-r}, \tag{21}$$

$$r = \frac{L}{L_*}, \tag{22}$$

$\mathbf{I}$ is the identity matrix, and $\mathbf{C}$ is the random-state matrix defined by Eq. (16). We see from Eq. (20) that w_L plays the role of relative weight between the two matrices corresponding to the respective asymptotic regimes in Eqs. (17) and (19). Note that the weights w_L obey the following group properties:

$$w_0 = 1, \quad w_\infty = 0, \quad \text{and} \quad w_{L_1}\, w_{L_2} = w_{L_1+L_2}. \tag{23}$$

It is also worth noticing that the transition matrix of the form Eq. (20) does not change the random state $\mathbf{c}$ and the matrix $\mathbf{C}$:

$$\mathbf{c}\mathbf{P} = \mathbf{c}, \quad \mathbf{C}\mathbf{P} = \mathbf{C}. \tag{24}$$

3. Formulation of continuous-value Markovian model

Our tests on realistic LES-generated cloud masks (presented in CSM2) showed very good agreement between the data statistics and the binary Markovian model predictions. This allows us to assume that the underlaying continuous-value fields (COT, LWP, etc.) can be also described by a Markovian statistical model. In this section we will describe general properties of such a model and present a specific form of it consistent with binary models of cloud masks derived from continuous-value fields.

a. General properties

In continuous-value Markovian model the stochastic 1D-field τ is defined on real line $\mathbb{R}$ and can take positive values within $[0, \tau_{\max}]$, where the upper bound $\tau_{\max}$ can be chosen arbitrary large but is naturally finite ($\tau_{\max} = \infty$ can be used to

simplify analytical computations). The generalization to 2D fields can be performed, as in the binary model, using the statistical ensemble of 1D transects. The field τ can be sampled on intervals of a finite length L, and the corresponding L-dependent statistics can be derived.

The stochastic state $(u\ v)$, which can be considered as a probability function defined on the binary set, is replaced in the continuous-value model by a normalized probability density function $\eta(\tau)$ defined on $[0, \tau_{\max}]$ and associated with the location x. The condition $u + v = 1$ corresponds to the normalization condition for $\eta(\tau)$:

$$\int_0^{\tau_{\max}} \eta(\tau) d\tau = 1. \tag{25}$$

When the state value is exactly known to be τ_0 the probability density has a δ-function form:

$$\eta(\tau) = \delta(\tau - \tau_0). \tag{26}$$

The analog of the binary-model random state $\mathbf{c} = (\bar{c}\ \bar{s})$ is the global distribution density $\rho(\tau)$ normalized by the condition

$$\int_0^{\tau_{\max}} \rho(\tau) d\tau = 1. \tag{27}$$

In the case of broken clouds it can be partitioned into a regular in-cloud part $\rho_{\mathrm{cld}}(\tau)$ and the singular part $\delta(\tau)$ corresponding to gaps between clouds (where $\tau = 0$):

$$\rho(\tau) = \rho_{\mathrm{tot}}(\tau) = \nu \rho_{\mathrm{cld}}(\tau) + (1 - \nu)\delta(\tau). \tag{28}$$

Here ν is the "absolute" cloud fraction (independent of cloud/clear separation setup). We assume that ρ_{cld} is normalized by the same condition Eq. (27) as $\rho(\tau)$. The moments of $\rho_{\mathrm{tot}}(\tau)$ and $\rho_{\mathrm{cld}}(\tau)$ are obviously related:

$$\langle \tau^n \rangle_{\mathrm{tot}} = \nu \langle \tau^n \rangle_{\mathrm{cld}}. \tag{29}$$

Below we will omit the subscript "tot" when this does not cause confusion.

The binary transition probability matrix $\mathbf{P}(L)$ from Eq. (7) is replaced in continuous-value model by the integral operator $\mathcal{P}_L$ with the kernel $P_L(\tau_1,\tau_2)$ which determines the probability of the transition from the interval $[\tau_1, \tau_1 + d\tau]$ at the point x to that of $[\tau_2, \tau_2 + d\tau]$ at $x + L$. We assume homogeneity of the model, so $\mathcal{P}_L$ is independent from x and depends only on the lag L. The transition between the state vectors η_1 at x and η_2 at $x + L$ is defined as

$$\eta_2(\tau_2) = \int_0^{\tau_{\max}} \eta_1(\tau_1) P_L(\tau_1, \tau_2) d\tau_1. \tag{30}$$

The binary row-sum relations in Eq. (8) have natural analog in continuous-value case, meaning that a transition occurs from a given value τ_1 at x to some value τ_2 at $x + L$ with unit probability; thus,

$$\int_0^{\tau_{\max}} P_L(\tau_1, \tau_2) d\tau_2 \equiv 1. \tag{31}$$

This condition can be used together with Eq. (30) to show that the final distribution $\eta_2(\tau_2)$ is normalized to unity as in Eq. (25).

The first group property Eq. (17) in continuous-value model becomes

$$P_0(\tau_1, \tau_2) = \delta(\tau_1 - \tau_2), \tag{32}$$

while the continuous-value analog of the second group property in Eq. (18) has the form of convolution:

$$P_{L_1+L_2}(\tau_1, \tau_2) = \int_0^{\tau_{\max}} P_{L_1}(\tau_1, \tau') P_{L_2}(\tau', \tau_2) d\tau'. \tag{33}$$

In the limit case of $L \to \infty$ the expression for the transition operator kernel is the generalization of Eq. (19):

$$P_\infty(\tau_1, \tau_2) = \rho(\tau_2). \tag{34}$$

In this case Eq. (30) coupled with the normalization condition Eq. (25) yields $\eta_2(\tau_2) = \rho(\tau_2)$ meaning that the value of τ_2 at infinity is independent from τ_1 and is just randomly chosen from the general PDF.

b. *Specific form of the transition operator*

We would like to generalize the binary transition matrix Eq. (20) to the continuous-value case by following the rule that the general expression is a weighted average of its limit cases (no value change at $L \to 0$ and random value choice at $L \to \infty$). The resulting expression of the transition operator kernel is

$$P_L(\tau_1, \tau_2) = w_L \delta(\tau_1 - \tau_2) + (1 - w_L)\rho(\tau_2), \tag{35}$$

where the weights $w_L = \exp(-L/L_*)$ are the same as in the binary model's Eq. (21). Here L_* is the scale (or autocorrelation) length of the continuous-value model. We will show below that the scale lengths of all binary cloud-mask models derived from a single continuous-value model are the same and coincide with L_* of this model. This means that the continuous-value model's L_* can be obtained from any derived binary model according to the procedures outlined in section 2, or independently from the autocorrelation function (see section 6 below).

Note that in the binary case the transition matrix, Eq. (20), is uniquely determined by the group and limit case requirements in Eqs. (17)–(19) (see appendix A). However, we cannot currently say the same about the transition operator kernel, Eq. (35), and the conditions (32)–(34). We will examine the possibilities to generalize Eq. (35) in our future work.

We will now show that the operator defined by Eq. (35) satisfies the Markovian properties, thus, in fact is a transition operator. The row-sum property Eq. (31) directly follows from Eq. (27):

$$\int_0^{\tau_{\max}} P_L(\tau_1, \tau_2) d\tau_2 = w_L + (1 - w_L) \int_0^{\tau_{\max}} \rho(\tau_2) d\tau_2 = 1. \tag{36}$$

The first group property, Eq. (32), and the limit condition, Eq. (34), are both obvious when w_0 is set to 1 and 0,

respectively, in Eq. (35). The second group property, Eq. (33), is also satisfied:

$$\begin{aligned}\int_0^{\tau_{\max}} P_{L_1}(\tau_1,\tau')P_{L_2}(\tau',\tau_2)d\tau' &= w_{L_1}w_{L_2}\delta(\tau_1-\tau_2)+(1-w_{L_1}w_{L_2})\rho(\tau_2),\\ &= w_{L_1+L_2}\delta(\tau_1-\tau_2)+(1-w_{L_1+L_2})\rho(\tau_2)\\ &= P_{L_1+L_2}(\tau_1,\tau_2)\end{aligned}. \tag{37}$$

Here we used a bit lengthy but straightforward algebraic computations and Eq. (23). Summarizing the above described properties, we conclude that Eq. (35) represents a continuous-value Markovian model characterized by the normalized value density $\rho(\tau)$ and the characteristic scale L_*.

Analogously to binary model's Eq. (24), the continuous-value transition operator of the form Eq. (35) leaves the random state intact:

$$\int_0^{\tau_{\max}} \rho(\tau_1)P_L(\tau_1,\tau_2)d\tau_1 = \rho(\tau_2). \tag{38}$$

Application of the transition operator to a state with definite COT value Eq. (26) yields

$$\begin{aligned}\eta(\tau_2) &= \int_0^{\tau_{\max}} \delta(\tau_1-\tau_0)P_L(\tau_1,\tau_2)d\tau_1\\ &= w_L\delta(\tau_2-\tau_0)+(1-w_L)\rho(\tau_2).\end{aligned} \tag{39}$$

This means that given a COT value at point x, selection of the value at point $x + L$ falls into two cases with the probabilities w_L and $(1 - w_L)$, respectively. In the first case $\tau(x + L)$ remains the same as $\tau(x)$, while in the second case it is randomly taken from the global probability distribution $\rho_{\text{tot}}(\tau)$.

4. Functional form of the COT PDF

We adopted gamma distribution as the functional form of non-zero-value COT PDF $\rho_{\text{cld}}(\tau)$. This assumption is based on observations of COT in marine boundary layer clouds (Barker 1996; Barker et al. 1996; Pincus et al. 1999) and our own analyses of airborne remote sensing measurements presented in section 8 below. Gamma distribution also provides good parameterization for COT histograms from LES-modeled trade wind cloud fields used in CSM2. In GISS GCM ModelE3 gamma distribution has been used as PDF for in-cloud water content following Morrison and Gettelman (2008).

We use the parameterization of gamma distribution function introduced by Hansen and Travis (1974) as a model for aerosol/cloud particle size distributions. In this notation adapted to COT the PDF has the following form:

$$\rho_{\text{cld}}(\tau) = \frac{(ab)^{(2b-1)/b}}{\Gamma[(1-2b)/b]}\,\tau^{(1-3b)/b}e^{-\tau/ab}, \tag{40}$$

where $a > 0, 0 < b < 1/2$, and $\Gamma(z)$ is the gamma function:

$$\Gamma(z) = \int_0^\infty t^{z-1}e^{-t}dt. \tag{41}$$

The parameters a and b have the respective meanings of the effective COT τ_{eff} and the effective variance υ_{eff} of the PDF:

$$a = \tau_{\text{eff}} = \frac{\langle\tau^3\rangle}{\langle\tau^2\rangle};\quad b = \upsilon_{\text{eff}} = \frac{\langle\tau^4\rangle\langle\tau^2\rangle}{\langle\tau^3\rangle^2} - 1. \tag{42}$$

Below we will use the notations (a, b) and $(\tau_{\text{eff}}, \upsilon_{\text{eff}})$ interchangeably since they are equivalent.

While the parameterization in Eq. (40) may not look familiar to someone outside the radiation modeling or remote sensing community, we refer our readers to appendix A of Alexandrov et al. (2018) where a and b are related to the parameters more common in other fields.

The first two moments of the COT PDF in Eq. (40) are

$$\langle\tau\rangle_{\text{cld}} = a(1-2b) \tag{43}$$

and

$$\langle\tau^2\rangle_{\text{cld}} = a^2(1-b)(1-2b), \tag{44}$$

respectively. Equation (43) can be used to derive the value of b after a is computed:

$$b = \frac{1}{2}\left(1 - \frac{\langle\tau\rangle_{\text{cld}}}{a}\right). \tag{45}$$

In some cases it is convenient to use the notation

$$\beta = \frac{1}{b} \tag{46}$$

($\beta > 2$), instead of b. For example, this simplifies Eq. (40):

$$\rho_{\text{cld}}(\tau) = \frac{(\beta/a)^{\beta-2}}{\Gamma(\beta-2)}\,\tau^{\beta-3}e^{-\beta\tau/a}. \tag{47}$$

5. Cloud masks

A binary cloud-mask Markovian model can be derived from a continuous-value one by selecting a cloud/clear separation threshold τ_{thr} and attributing the values of $\tau \geq \tau_{\text{thr}}$ to the class • (cloudy), while the values of $\tau < \tau_{\text{thr}}$ to the class ∘ (clear). For analysis of the dependence of cloud-mask statistics on the (brightness) threshold value for real satellite observations, see, e.g., Wielicki and Welch (1986).

a. *Cloud fraction*

In cloud-mask model derived from continuous-value model with the global COT PDF $\rho(\tau)$ of the form in Eq. (28) the global cloud fraction $\bar{c}$ and its clear-sky analog $\bar{s}$ are defined as

$$\bar{c} = \int_{\tau_{\text{thr}}}^{\tau_{\max}} \rho(\tau)d\tau = \nu\int_{\tau_{\text{thr}}}^{\tau_{\max}} \rho_{\text{cld}}(\tau)d\tau \tag{48}$$

and

$$\bar{s} = \int_0^{\tau_{\text{thr}}} \rho(\tau)d\tau = 1 - \nu + \nu\int_0^{\tau_{\text{thr}}} \rho_{\text{cld}}(\tau)d\tau, \tag{49}$$

respectively. The relation $\bar{c} + \bar{s} = 1$ follows directly from Eq. (27).

If $\rho_{\text{cld}}(\tau)$ has gamma-distribution functional shape in Eq. (47) the integral in Eq. (48) can be computed analytically yielding the following expression for $\bar{c}$:

$$\bar{c} = \nu \frac{\Gamma(\beta - 2, \beta\tau_{\text{thr}}/a)}{\Gamma(\beta - 2)}. \tag{50}$$

Here $\tau_{\max} = \infty$ is assumed for simplicity and

$$\Gamma(z, x) = \int_x^\infty t^{z-1} e^{-t} dt \tag{51}$$

is incomplete gamma function. The value of $\bar{c}$ can only decrease down from ν with the increase of τ_{thr}, since $\Gamma(z, x)$ is a decreasing function of x (with maximum at $x = 0$).

b. Markovian model of cloud mask

In this section we will show how cloud-mask binary Markovian model described in section 2 can be derived from the underlaying continuous-value model. Binary state $\mathbf{u} = (u\ v)$ can be obtained from the continuous-value state $\eta(\tau)$ by means of integration:

$$u = \int_{\tau_{\text{thr}}}^{\tau_{\max}} \eta(\tau) d\tau, \quad v = \int_0^{\tau_{\text{thr}}} \eta(\tau) d\tau. \tag{52}$$

The condition $u + v = 1$ follows from the normalization condition in Eq. (25) of $\eta(\tau)$. Any continuous-value state function $\eta(\tau)$ can be expressed as

$$\eta(\tau) = u\eta_\bullet(\tau) + v\eta_\circ(\tau), \tag{53}$$

where the states $\eta_\bullet(\tau)$ and $\eta_\circ(\tau)$ are continuous-value representations of the binary states $\bullet$ and $\circ$, respectively. As any state they are normalized to unity. Explicitly, $\eta_\bullet(\tau)$ is defined as

$$\eta_\bullet(\tau) = \begin{cases} \eta(\tau)/u, & \tau \in [\tau_{\text{thr}}, \tau_{\max}] \\ 0, & \tau \in [0, \tau_{\text{thr}}) \end{cases}, \tag{54}$$

normalized by

$$\int_0^{\tau_{\max}} \eta_\bullet(\tau) d\tau = \frac{1}{u} \int_{\tau_{\text{thr}}}^{\tau_{\max}} \eta(\tau) d\tau = 1. \tag{55}$$

Similarly, $\eta_\circ(\tau)$ is defined as

$$\eta_\circ(\tau) = \begin{cases} 0, & \tau \in [\tau_{\text{thr}}, \tau_{\max}] \\ \eta(\tau)/v, & \tau \in [0, \tau_{\text{thr}}) \end{cases}, \tag{56}$$

normalized by

$$\int_0^{\tau_{\max}} \eta_\circ(\tau) d\tau = \frac{1}{v} \int_0^{\tau_{\text{thr}}} \eta(\tau) d\tau = 1. \tag{57}$$

A transition in the binary model from the initial states $\bullet$ or $\circ$ associated with point x to another point $x + L$ corresponds in the underlaying continuous-value model to a transition from the states $\eta_\bullet$ or $\eta_\circ$, respectively. The result of this transition

$$\tilde{\eta}_i(\tau_2) = \int_0^{\tau_{\max}} \eta_i(\tau_1) P_L(\tau_1, \tau_2) d\tau_1, \tag{58}$$

($i = \circ, \bullet$) is not a "pure" $\bullet$ or $\circ$ state and can be decomposed according to Eq. (53) with the coefficients u and v playing the roles of the transition probabilities between the initial and final binary states:

$$P_{i\bullet} = \int_{\tau_{\text{thr}}}^{\tau_{\max}} \tilde{\eta}_i(\tau_2) d\tau_2 \quad \text{and} \quad P_{i\circ} = \int_0^{\tau_{\text{thr}}} \tilde{\eta}_i(\tau_2) d\tau_2, \tag{59}$$

$i = \circ, \bullet$. The row-sum property in Eq. (8)

$$P_{i\bullet} + P_{i\circ} = 1 \tag{60}$$

follows from the normalization condition for $\tilde{\eta}_i(\tau_2)$.

The explicit expressions for the elements of the cloud-mask transition matrix $\mathbf{P}(L)$ are computed according to Eqs. (58) and (59) in appendix B resulting to the expression

$$\mathbf{P}(L) = w_L \begin{pmatrix} 1 & 0 \\ 0 & 1 \end{pmatrix} + (1 - w_L) \begin{pmatrix} \bar{c} & \bar{s} \\ \bar{c} & \bar{s} \end{pmatrix}, \tag{61}$$

which is identical to the transition matrix of binary Markovian model in Eq. (20). Note that while the binary-model parameter $\bar{c}$ depends on the choice of the threshold τ_{thr}, the scale L_* is inherited from Eq. (35) through the weight w_L and, thus, is independent from τ_{thr} value.

We have demonstrated that the Markovian statistics of cloud masks derived from continuous-value model described by Eq. (35) are consistent with the binary Markovian model described in section 2 and CSM3.

6. Structure and autocorrelation functions

The notion of structure function (SF) quantifying the average change of the variable value over a lag L is common in atmospheric sciences (see, e.g., Davis et al. 1994; Lovejoy and Schertzer 2012) including our own works on atmospheric aerosols (Alexandrov et al. 2004, 2016b). Here we will use the second-order SF that is defined in 1D case as

$$S_2(L) = \langle [\tau(x + L) - \tau(x)]^2 \rangle, \tag{62}$$

where the averaging is taken over x and over all realizations in the ensemble. To derive the analytical form of SF from Eqs. (28), (35), and (40) we need to compute statistics $\langle (\tau_2 - \tau_1)^2 \rangle$, where $\tau_1 = \tau(x)$ is randomly taken from the global total distribution $\rho_{\text{tot}}(\tau)$(and can be zero), while $\tau_2 = \tau(x + L)$ is the result of application of the transition operator to τ_1. The averaging is then made over both τ_1 and τ_2 within their respective distributions.

The value of τ_1 is distributed according to $\rho(\tau)$, while τ_2 is distributed according to $\eta(\tau)$ from Eq. (39). This means that $\tau_2 = \tau_1$ [thus, $S_2(L) = 0$] with the probability w_L, while in the

opposite case (with the probability $1 - w_L$) τ_2 gets a random value taken from $\rho(\tau)$. The former case corresponds to the limit $L = 0$, while the latter corresponds to $L \to \infty$. This allows us to write the expression for SF in the following form:

$$S_2(L) = w_L S_2(0) + (1 - w_L) S_2(\infty). \tag{63}$$

Here $S_2(0) = 0$, while in the limit of infinite L the values of τ_1 and τ_2 are independent:

$$\mathrm{Cov}(\tau_1, \tau_2) = 0, \tag{64}$$

and identically distributed according to $\rho(\tau)$ with the mean $\langle\tau\rangle$. Thus, using Eq. (64) we obtain

$$\begin{aligned} S_2(\infty) &= \langle(\tau_2 - \tau_1)^2\rangle \\ &= \langle[(\tau_2 - \langle\tau\rangle) - (\tau_1 - \langle\tau\rangle)]^2\rangle = 2\mathrm{Var}_{\mathrm{tot}}(\tau), \end{aligned} \tag{65}$$

where all averages are taken with respect to the total distribution $\rho_{\mathrm{tot}}(\tau)$. Then the expression Eq. (63) for the SF takes the following form:

$$S_2(L) = 2\mathrm{Var}_{\mathrm{tot}}(\tau)(1 - e^{-L/L_*}). \tag{66}$$

The variance in Eq. (66) can be expressed in terms of the moments of the in-cloud distribution $\rho_{\mathrm{cld}}(\tau)$ using Eq. (29):

$$\begin{aligned} \mathrm{Var}_{\mathrm{tot}}(\tau) &= \langle\tau^2\rangle_{\mathrm{tot}} - \langle\tau\rangle^2_{\mathrm{tot}} \\ &= \nu\langle\tau^2\rangle_{\mathrm{cld}} - \nu^2\langle\tau\rangle^2_{\mathrm{cld}}. \end{aligned} \tag{67}$$

The expressions for the first and the second moments of $\rho_{\mathrm{cld}}(\tau)$ having gamma-distribution form in Eq. (40) are given by Eqs. (43) and (44), respectively. They yield the following expression for COT variance:

$$\mathrm{Var}_{\mathrm{tot}}(\tau) = \nu a^2(1 - 2b)[\nu b + (1 - \nu)(1 - b)], \tag{68}$$

and the final expression for the structure function:

$$\begin{aligned} S_2(L) = 2\nu a^2 b(1 - 2b)[\nu b + (1 - \nu)(1 - b)] \\ \times (1 - e^{-L/L_*}). \end{aligned} \tag{69}$$

Note that at small lags $S_2 \propto L$ corresponding to the Hurst exponent $H = 1/2$ (generally, $S_2 \propto L^{2H}$). This value of H corresponds to classical Brownian motion, which is a Markovian random process, so this result is expected as being derived from a Markovian COT model.

In a model with the global mean $\langle\tau\rangle$ and the variance $\mathrm{Var}(\tau)$ the autocorrelation function (AF) is defined as

$$W(L) = \frac{\langle[\tau(x) - \langle\tau\rangle][\tau(x + L) - \langle\tau\rangle]\rangle}{\mathrm{Var}(\tau)}. \tag{70}$$

It is related to the second-order structure function:

$$S_2(L) = 2\mathrm{Var}_{\mathrm{tot}}(\tau)[1 - W(L)]. \tag{71}$$

Comparison of this expression with Eq. (66) yields

$$W(L) = e^{-L/L_*}, \tag{72}$$

which is independent from the COT distribution $\rho_{\mathrm{tot}}(\tau)$. Expectedly, $W \to 0$ as $L \to \infty$, while $W \to 1$ as $L \to 0$. Equation (72) demonstrates that L_* is indeed the autocorrelation length of the model and gives a new meaning to the weights w_L entering the expressions for the binary transition matrix in Eq. (20) and the continuous-value transition operator's kernel in Eq. (35).

7. Construction of examples

Examples (realizations) of the continuous-value Markov process described by the transition operator with the kernel Eq. (35) can be constructed using the following simple sequential algorithm based on Eq. (39). Given the model parameters ν, L_*, and $\rho_{\mathrm{cld}}(\tau)$, one should first specify the resolution l of the realization and compute the probability

$$w(l) = e^{-l/L_*}. \tag{73}$$

This parameter is also the value of the model's autocorrelation function at the scale l. Then, the initial value τ_0 of the realization is chosen by picking it at random from the distribution $\rho(\tau)$. To do this we first determine if this point is cloudy or clear by "flipping a coin" with probability ν for cloudy. If the result is "clear" then $\tau_0 = 0$; otherwise, we chose τ_0 from the distribution $\rho_{\mathrm{cld}}(\tau)$of the positive COT values. A simple way to do this starts with generation of two random numbers z_τ and z_ρ on the unit interval (0, 1). Then the first is used to get random $\tau_0 = z_\tau\tau_{\max}$, and the second is used to get a random value in the distribution dimension $\rho_0 = z_\rho\max(\rho_{\mathrm{cld}})$. Then, if $\rho_0 \leq \rho_{\mathrm{cld}}(\tau_0)$ [i.e., if the point (τ_0, ρ_0) is below the curve $\rho_{\mathrm{cld}}(\tau)$] the random value τ_0 is declared the result of the trial; otherwise, the trial is discarded and the procedure is repeated again.

Given the value τ_i at the ith step of the procedure, the next value τ_{i+1} is chosen in the way outlined in Fig. 1. First, we "flip a coin" returning 1 with the probability $w(l)$ and 0 with the probability $1 - w(l)$. If the result is 1, then $\tau_{i+1} = \tau_i$ [corresponding to the first term in Eq. (39)]. If the result is 0, then τ_{i+1} is randomly taken from the distribution $\rho_{\mathrm{tot}}(\tau)$ in the same way as it was described above for choosing of the initial value τ_0. This corresponds to the second term in Eq. (39).

The described algorithm produces stationary piecewise constant curves which, unlike real COT patterns, do not exhibit any trends. While in most of the cases our model is physically adequate, in some instances (see section 8) a trend has to be added manually. Among future developments of our model we consider its merger with the classical Brownian motion (which is also Markovian) in order to accommodate for random trends and replace constant-COT intervals with something more realistic.

To test the algorithm described above we generated a dataset with the following parameters:

$$\nu = 0.91, \quad L_* = 448\ \mathrm{m}, \quad \tau_{\mathrm{eff}} = 32, \quad \upsilon_{\mathrm{eff}} = 0.39. \tag{74}$$

They are consistent with an LES dataset used in CSM2 for evaluation of our binary cloud-mask model. That simulation

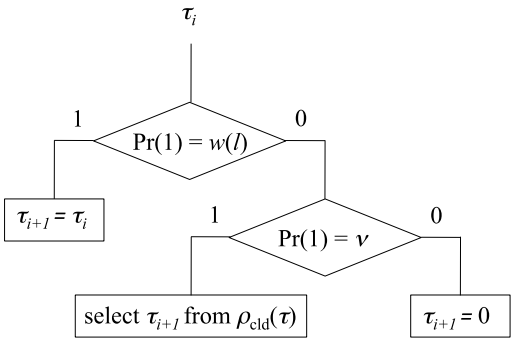

FIG. 1. Flowchart of the realization generation algorithm.

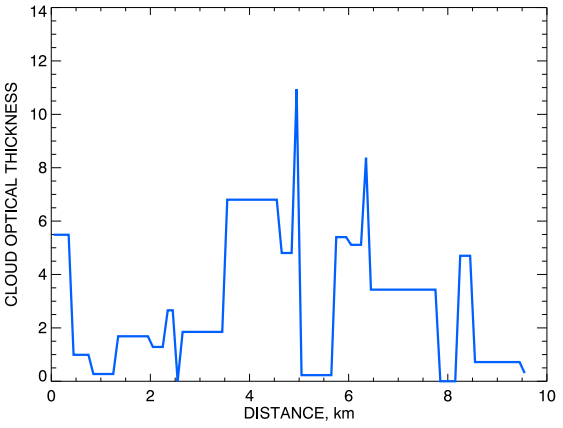

FIG. 2. An example of COT segment from the ATEX imitation dataset generated using our Markovian model. The parameters of the model are defined by Eq. (74).

was performed using the LES model described by Ackerman et al. (2004) and was based on the Atlantic Tradewind Experiment (ATEX; Stevens et al. 2001) focusing on cumulus clouds rising into a thin stratocumulus layer. Only the first 12 scenes (corresponding to 0400–0645 h of the day) were used in CSM2 to preserve homogeneity of the statistical ensemble. While the scenes of the ATEX LES dataset were computed on 2D grid, the CSM2 analysis was performed on their 1D transects parallel to their E–W and S–N axes. The number of these transects was $2 \times 96 \times 12 = 2304$. The sample size and the resolution were $L = 9.6$ km and $l = 100$ m, respectively.

The parameterization in Eq. (74) was used to initiate the process described in the beginning of this section to produce an ensemble of realizations of the corresponding Markovian COT model. Hereafter we will refer to our statistically generated dataset as "ATEX imitation" to distinguish it from the dynamical model's "simulation." The same sample size and spatial resolution as in the LES dataset were used. While realizations of the Markovian model can be generated only in 1D, the number of independent 1D samples in the imitation dataset was made equal to the total number of the transects in the LES dataset. Figure 2 shows a randomly chosen COT segment of the ATEX imitation dataset.

Statistical comparison of our imitations with the LES datasets themselves and discussion of their differences will be presented in the upcoming Part II of this series. Here we are only interested in how well the statistics of the generated dataset agree with the theoretical results described earlier in the paper. This algorithm performance evaluation was conducted in the following three ways. First, we checked how well the COT PDF derived from the dataset agrees with the gamma distribution used to generate it. Second, we compared the dataset's cloud-mask statistics corresponding to four COT thresholds (0.1, 1, 10, and 30) to the theoretical laws based on Eq. (50) for CF and Eq. (3) for $L_\bullet$ and $L_\circ$, while L_* values from these cloud masks should be threshold independent and close to 448 m from Eq. (74). Third, we compared the structure and autocorrelation functions derived from the generated data to these theoretically computed using Eqs. (69) and (72), respectively.

The COT PDF derived from the ATEX imitation dataset is shown in Fig. 3 (with its exponential "tail" shown in log scale in right panel). The black curve represents the gamma-shaped distribution, Eq. (40), with the parameters $\tau_{\text{eff}} = 31.2$ and $\nu_{\text{eff}} = 0.38$ derived from the COT moments using Eqs. (42) and (45). These parameters are very close (within 2.5%) to the corresponding Eq. (74) values, and the COT PDF derived from the generated dataset appears to be practically identical (with some inevitable random noise) to the gamma-distribution PDF that was used for its generation.

The cloud-mask statistics of the ATEX imitation dataset were derived following the algorithm outlined in CSM2. First, we used the data samples to collect the lengths of cloudy and clear intervals (for given τ_{thr}). Then, the mean cloud and gap lengths were derived from these collections. These two values were subsequently corrected according to Eq. (4) for finite-sample size L resulting in the "infinite-sample" values of $L_\bullet$ and $L_\circ$, respectively. These parameters then were used to compute the scale length L_* according to Eq. (1). On the next step, L_* was corrected for the model's finite resolution l according to Eq. (6), and its adjusted value was used in Eq. (3) to obtain the resolution-corrected $L_\bullet$ and $L_\circ$. The cloud fraction $\bar{c}$ is not biased by either the finite sample size or the resolution (see CSM1, CSM2, and CSM4). It was computed directly as the ratio of the number of cloudy pixels in the whole dataset to the total number of pixels there.

Figure 4 shows plots of $\bar{c}$, L_*, $L_\bullet$, and $L_\circ$ as functions of the COT threshold τ_{thr}. The corresponding theoretical dependances are shown by green lines: from Eq. (50) for $\bar{c}$ in Fig. 4 (top left) and Eq. (3) for $L_\bullet$ and $L_\circ$ in Fig. 4 (bottom, left and right, respectively). Diamonds there depict the statistics corresponding to the thresholds of 0.1, 1, 10, and 30 (green: theoretical; blue: derived from the imitation dataset). We see that in all four panels the values from the imitation dataset are practically identical to the corresponding theoretical values. In particular, the imitation-dataset values of L_* in Fig. 4 (top right) are indeed threshold independent.

Figure 5 demonstrates that the autocorrelation and structure functions of the imitation dataset also coincide with their theoretical predictions in Eqs. (72) and (69), respectively. The

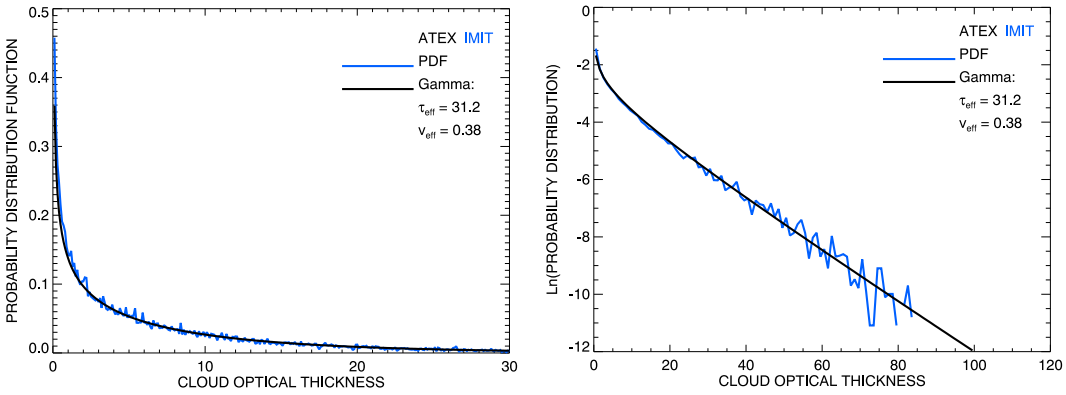

FIG. 3. COT probability distribution functions for the ATEX imitation dataset. (right) The *y* axis is in a logarithmic scale to show exponential asymptotic behavior. The gamma-function model PDF is shown in black.

above comparisons demonstrate the robustness of the algorithm described in this section.

8. Examples from real-life RSP datasets

In this section we will demonstrate the ability of our Markovian model to parameterize a variety of real COT datasets and to generate synthetic data with the same statistical properties. For this purpose we use the COT retrievals made from the RSP measurements during two field campaigns. The observed cloud fields include Cu, Sc, and As.

The RSP is an airborne along-track scanner with high angular resolution of 14 mrad FOV. It makes measurements at 0.8° intervals within ±60° from nadir. The scanning is continuous with 0.8 s per scan. The translation of these parameters into spatial resolutions of the RSP datasets depends on the speed

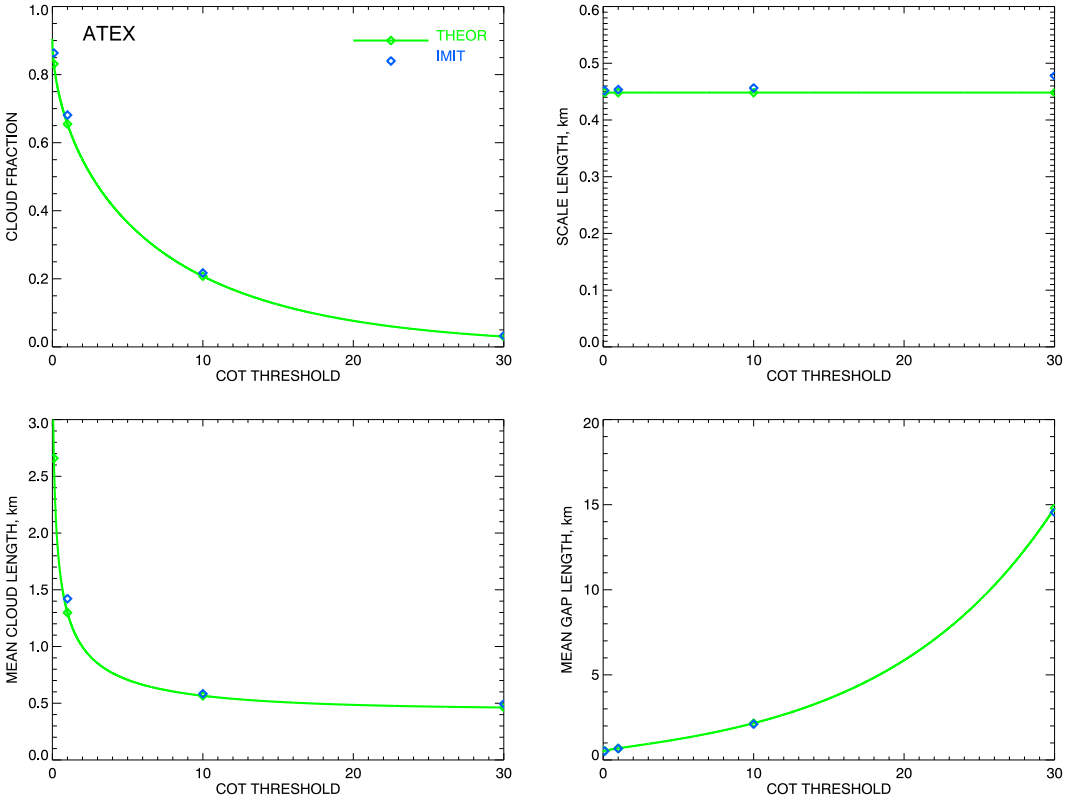

FIG. 4. Cloud-mask statistics from the ATEX imitation dataset as functions of COT threshold: (top left) cloud fraction $\bar{c}$, (top right) scale length L_*, (bottom left) mean cloud length $L_\bullet$, and (bottom right) mean gap length $L_\circ$. The theoretical dependances are shown by green lines. Diamonds depict statistics corresponding to the cloud–clear separation thresholds of 0.1, 1, 10, and 30 (green: theoretical; blue: derived from the imitation dataset).

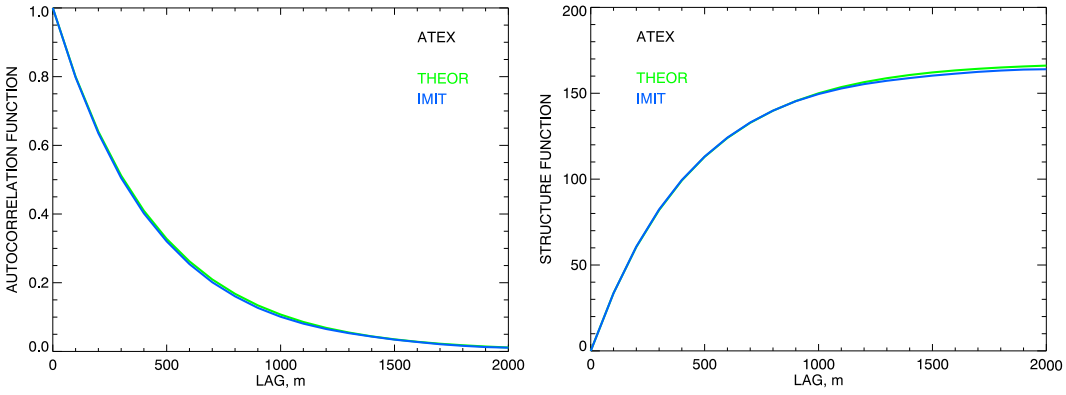

FIG. 5. (left) Autocorrelation functions in Eq. (70) for ATEX imitation dataset (blue) and the theoretical function in Eq. (72) (green). (right) As in the left panel, but for second-order structure functions, Eq. (62); the theoretical curve is from Eq. (69).

and the altitude of the aircraft (Alexandrov et al. 2016a). It can range from about 200 m for NASA's high-altitude ER-2 flying with the speed of 210 m s^{-1} at 20 km above ground down to less than 100 m for more conventional airplanes (P3-B, B-200, UC-12, C-130) usually making about 120 m s^{-1} at 5–7-km altitude. The resolution of RSP's cloud products may change during the flight with changing speed, altitude, and the cloud-top height beneath the aircraft.

The RSP has been deployed in numerous NASA field campaigns during the past decades (see, e.g., Alexandrov et al. 2015, 2016a,c, 2018; Sinclair et al. 2017, 2019).

The COT retrievals from RSP-measured total reflectances at nadir view are made using a modification of the widely used bispectral technique (Nakajima and King 1990). In the modified algorithm no absorbing spectral channels are used while the droplet effective radius is derived from the polarized reflectance in the rainbow (cloud bow) scattering range between 137° and 165° (Alexandrov et al. 2012). Then, the COT value is determined from lookup table built for nonabsorbing 863-nm channel using plain-parallel radiative transfer computations. As the original bispectral technique, this method can produce biases in COT values in the presence of 3D radiative effects (such as light escape from broken cloud sides or shadowing at low sun angles). However, in this study we do not address such biases and consider the RSP-derived COTs as true records subject to statistical parameterization and imitation.

A problem common to most statistical analyses using real-life data is in keeping the balance between homogeneity of the dataset (so it should be small enough for its statistical properties not to change within it) and the data volume sufficiently large for derivation of reliable statistics. While we have not yet implemented a rigorous procedure for estimation of statistical homogeneity of the sample, we currently relay on visual analysis of the COT pattern and also on how well the COT PDF can be fitted by a relatively narrow gamma distribution. A prospective algorithm for quantification of the sample homogeneity can be based on comparison between the statistics of different subsamples.

In the case of aerial overpass above a rapidly changing cloud field we can obtain a conclusive analysis only if the field's statistics do not change or change much slower than the field itself (e.g., clouds move but do not disappear all together). On the other hand, in the case of geostationary satellite observations (e.g., Seelig et al. 2021) 2D spatial COT fields can be derived independently for any moment of the cloud system evolution. These 2D snapshots (if sufficiently large and homogeneous) can be used for derivation of all four parameters of our model. This is a rather simple statistical procedure outlined for 1D case in the next paragraph, so unlike Seelig et al. (2021) we do not need to track individual clouds. The model parameters then can be combined into time series reflecting the evolution of the cloud field. For example, in a simple case of evaporating cloud system such time series are expected to behave similarly to the curves in Fig. 4 (if the threshold in COT on x axis is replaced by the COT value lost due to evaporation): CF declines, clouds become smaller on average (some probably disappear) and the gaps between them increase in size. The effective COT should also decline.

Below we present examples of analysis and imitation of the RSP COT retrievals from selected cases with long flight legs over statistically homogeneous (in the above-described sense) cloud fields. The parameterizations of these cloud fields were made using the methodology similar to that applied to the imitated ATEX dataset at the end of section 7. The PDF parameters τ_{eff} and v_{eff} were derived from the COT moments using Eqs. (42) and (45). The cloud fraction ν was computed as the ratio between the number of pixels determined as cloudy by the RSP algorithm (basing on the presence of cloud bow in the polarized reflectance) to the total number of pixels in the selected interval. The scale length L_* was derived from the COT's autocorrelation function assuming that it has the form in Eq. (72). The Markovian model's parameters derived from the four datasets described in this section are presented in Table 1. They were used for generation of the corresponding imitations according to the algorithm described in section 7.

TABLE 1. Cloud field parameters for four RSP examples.

ν (%)	L_* (m)	τ_{eff}	v_{eff}	$\langle\tau\rangle$	$\sigma(\tau)$	h_{top} (m)
Cu: RACORO, 1419–1430 UTC 5 Jun 2009, 92 km, 751 points						
6.7	297	7.3	0.02	7.1	0.9	400
Sc: RACORO, 1435–1459 UTC 5 Jun 2009, 195 km, 988 points						
79.3	349	6.0	0.04	5.5	1.1	500
As: PODEX, 1956–2014 UTC 1 Feb 2013, 226 km, 1311 points						
90.1	6582	3.1	0.17	2.2	1.2	8200
Sc[a]: PODEX, 1852–1909 UTC 3 Feb 2013, 209 km, 1201 points						
100	1297	20.6	0.02	19.7	3.1	200

[a] With the trend in COT removed.

a. *RACORO: Cu-to-Sc transition*

The first couple of examples are from the 2009 field campaign Routine Atmospheric Radiation Measurement (ARM) Aerial Facility (AAF) Clouds with Low Optical Water Depth (CLOWD) Optical Radiative Observations (RACORO) coordinated by the AAF (Vogelmann et al. 2012). The campaign was held in Oklahoma's southern Great Plains from January to June 2009. The RSP was on board NASA's B-200 aircraft. At this part of the year there are plenty of "popcorn" cumulus clouds in this area forming vast and statistically homogeneous fields suitable for our analysis. Both examples presented here are from the same long leg flown on 5 June 2009. While the two selected intervals are adjacent to each other (1418:58–1429:45 and 1435:06–1458:44 UTC) they have different cloud field structures: the small-size Cu clouds in the first part (Fig. 6) later gave way to a Sc field with frequent gaps (Fig. 7). The cloud-top heights in both cases were between 400 and 500 m. The cloud-field parameters presented in Table 1 show that the Cu-to-Sc transition results in small decrease in the mean and effective COTs by about 1 (from 7 to 6), while the COT PDF remains narrow (v_{eff} = 0.02–0.04) and well-represented by gamma distribution (see bottom-right panels of Figs. 6 and 7). The autocorrelation length L_* moderately increased during the transition (from around 300 to 350 m), while the most dramatic change occurred in the cloud fraction ν: an increase from 7% to 79%. The results of Markovian model's imitations are presented in top-right panels of Figs. 6 and 7. They are compared to the actual COT measurements (from top-left plots) in bottom-left panels (within shorter intervals for better clarity). As a result of both actual and simulated datasets having the same

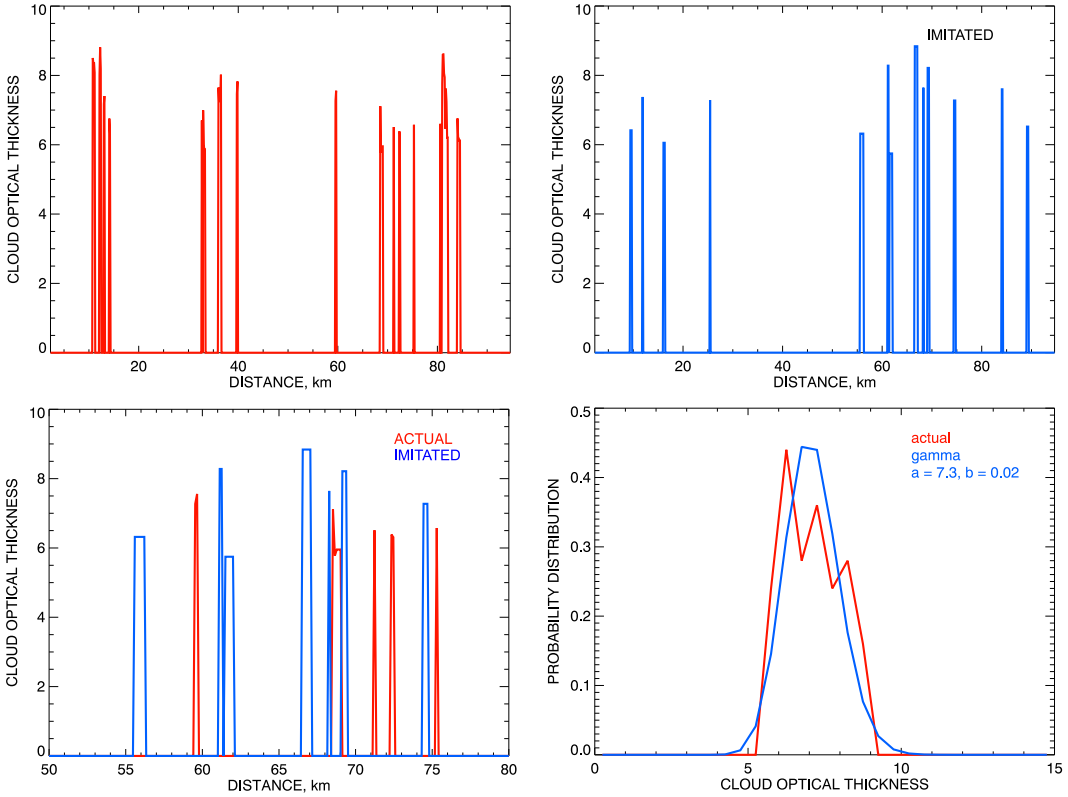

FIG. 6. (top left) Cu COT derived from the RSP measurements made during RACORO field campaign between 1418:58 and 1429:45 UTC 5 Jun 2009. (top right) Imitated COT based on the statistics of the field in the top-left panel. (bottom left) Zoom-in on both datasets at the middle of the interval (note that the simulated COT is expected to be similar to the original only statistically, not point by point). (bottom right) PDF of the nonzero COT (red) and its fit with the gamma distribution (blue). Here a and b stand for τ_{eff} and v_{eff}, respectively; see Eq. (42).

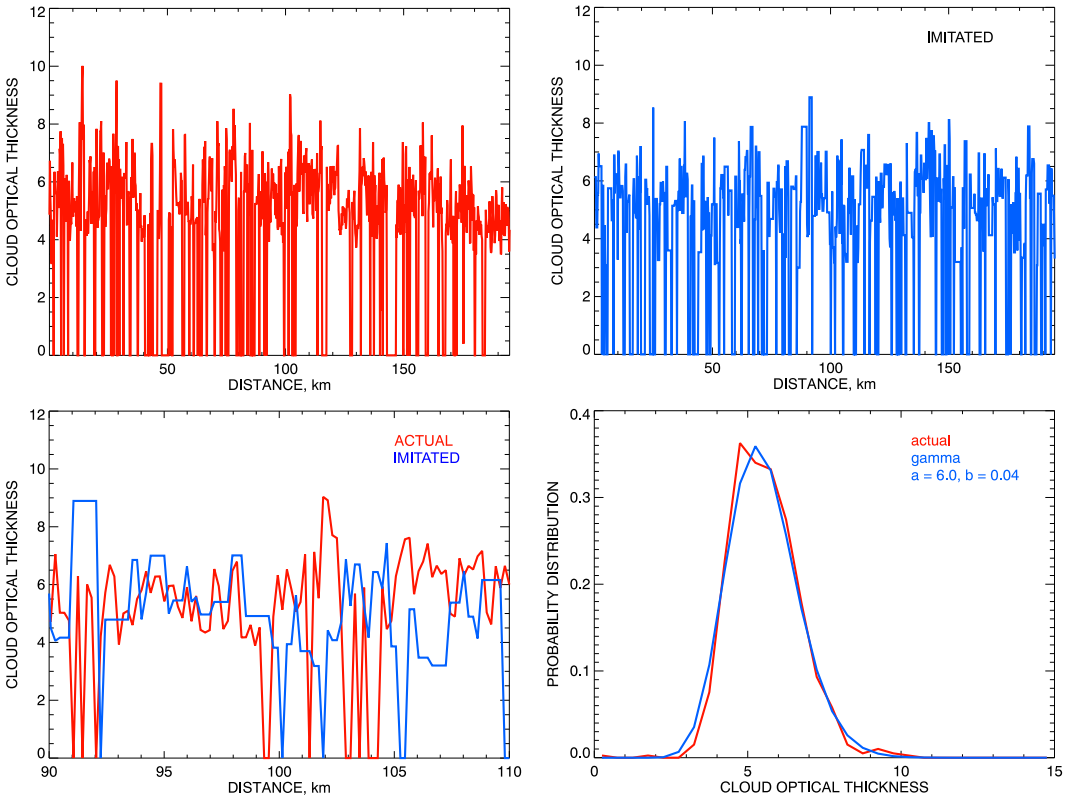

FIG. 7. As in Fig. 6, but for the RSP measurements made between 1435:06 and 1458:44 UTC 5 Jun 2009.

statistics, these comparisons show visual similarities in the structure of COT curves (while no point-by-point matching can be expected).

b. *PODEX: Marine stratocumulus and altostratus clouds*

The next two examples had been selected from the RSP dataset obtained during the Polarimeter Definition Experiment (PODEX) held between 14 January and 6 February 2013. The NASA ER-2 airplane carrying the RSP was based at NASA Dryden (now Armstrong) Aircraft Operation Facility in Palmdale, California, north from Los Angeles. The retrievals of cloud properties from the RSP measurements were performed for both the California Valley and the coastal waters (Alexandrov et al. 2015).

The first example from PODEX (presented in Fig. 8) is a marine stratocumulus deck observed off the California coast between 1852:11 and 1909:00 UTC 3 February 2013. This was an overcast ($\nu = 0$) low-altitude cloud with an average cloud-top height of only 200 m. Figure 8 (top left) shows a pronounced mostly linear trend in COT, which cannot be characterized or simulated within the current framework of our statistical model (see section 7). This is an example of nonhomogeneous sample where the local mean COT (and therefore the local PDF) is changing with the location leading to a wide nongamma global PDF. Thus, we approximated this trend by a linear function and subtracted it from the COT data before performing statistical analysis. Figure 8 (bottom right) showing how closely the real (while detrended) COT PDF is approximated by gamma distribution with $\tau_{\text{eff}} = 21$ and $\upsilon_{\text{eff}} = 0.02$. The autocorrelation length $L_* \approx 1300$ m in this case is quite large compared to the RACORO examples presented above. We used these statistics of the detrended dataset to imitate the stationary COT pattern. After this we added the linear trend back yielding the curve presented in Fig. 8 (top right). It looks quite similar to the actual COT pattern while (by construction) having a simpler trend structure. A zoom-in in Fig. 8 (bottom left) presenting both real and imitated COTs in the same plot shows statistical similarity in their small-scale variability.

Figure 9 presents our second example from PODEX: an altostratus (As) cloud observed between 1955:41 and 2014:04 UTC 1 February 2013. This high-altitude cloud with top height of 8.2 km is quite different from those in the previous examples of boundary layer clouds. There are only few gaps in this cloud ($\nu \approx 90\%$) and it is rather thin ($\tau_{\text{eff}} = 3.1$, $\langle\tau\rangle = 2.2$). At the same time, it has a wide COT PDF shown in Fig. 9 (bottom right) with $\upsilon_{\text{eff}} = 0.17$ (4–8 times larger than in the Cu and Sc examples). This reflects the volatile nature of the COT seen in Fig. 9 (top left). This PDF still can be approximated by gamma distribution reasonably well (while not as well as in the other examples). Another distinctive feature of this cloud is the large autocorrelation length of 6.6 km (substantially exceeding not only $L_* \sim 300$ m in the RACORO examples, but also $L_* \sim 1.3$ km in the PODEX Sc case). This makes the COT

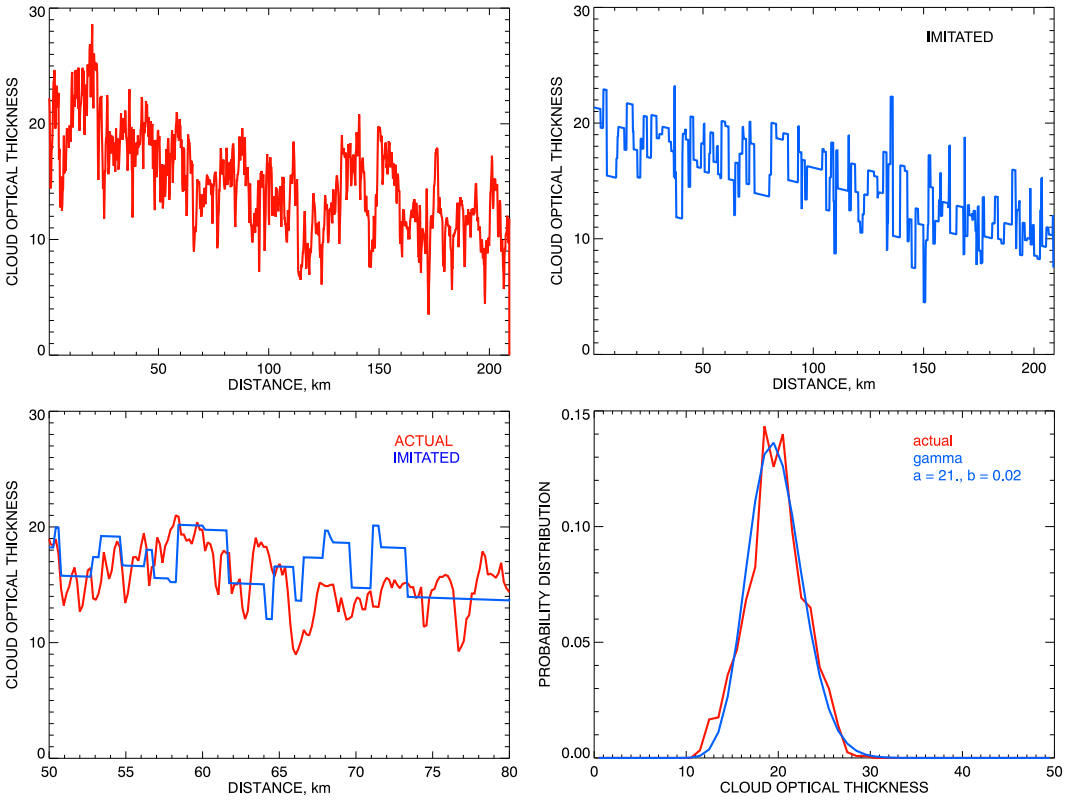

FIG. 8. As in Fig. 6, but for the RSP observations of Sc deck made during PODEX between 1852:11 and 1909:00 UTC 3 Feb 2013.

curve in Fig. 9 (top left) look more "continuous." This curve also shows a degree of nonstationarity common to Brownian motions, while not represented in our statistical model. This explains the visible difference in variability between the actual COT pattern in Fig. 9 (top left) and the imitated one in Fig. 9 (top right). On smaller spatial scales the agreement is better, as shown in Fig. 9 (bottom left), while the imitation curve lacks small-scale fluctuations present in the measurements. This example indicates that the performance of the current statistical cloud model depends on cloud type and further efforts are needed to adapt it to a wider range of different cloud fields.

9. Discussion of cloud scale

While cloud fraction is a standard data product for many satellite instruments, and COT histograms are being stored (e.g., on 1° × 1° grid in MODIS data collection; King et al. 2013), the cloud-scale statistics still deserve more attention by scientific community. The existing observational studies of cloud scale fall into two main categories: derivation of cloud size (area or chord length) distributions and autocorrelation/power-spectrum analysis of COT fields. Various types of data were used: ground based, airborne, and satellite; optical or radar measurements. Our model covers both approaches since we describe both (threshold-dependent) cloud mask statistics and autocorrelation and structure functions. Note that the small-scale behavior of the latter is related to that of the power spectrum (see, e.g., Davis et al. 1994; Alexandrov et al. 2004).

A number of studies have been published describing cloud chord statistics based on ground-based measurements (e.g., Lane et al. 2002; Berg and Kassianov 2008) as well as aircraft and satellite data (e.g., Plank 1969; Cahalan and Joseph 1989; Rodts et al. 2003). Some of these studies report exponential cloud and gap chord length distributions (Astin and Latter 1998; Lane et al. 2002), while others find power-law distributions (Cahalan and Joseph 1989; Koren et al. 2008; Wood and Field 2011; Dorff et al. 2022). Joseph and Cahalan (1990) found the gap length ("nearest neighbor spacing") distribution to be close to a combination of Weibull and lognormal functional shapes. In our approach (see CSM1) the distributions of both cloud and gap chord lengths are exponential with the mean values $L_\bullet$ and $L_\circ$, respectively [related to the model parameters CF and L_* via Eq. (3)]. However, we demonstrated in CSM2 that in the case of a diverse sample (where the parameters $L_\bullet$ and $L_\circ$ are themselves statistically distributed) the cloud and gap length distributions have a power-law shape. This is particularly characteristic for long-term observations on global scale (e.g., Wood and Field 2011).

Another type of studies of COT inhomogeneity is based on autocorrelation functions and power spectrum analysis. Schäfer et al. (2017) computed 1D and 2D autocorrelation functions of COT fields derived from ground-based and

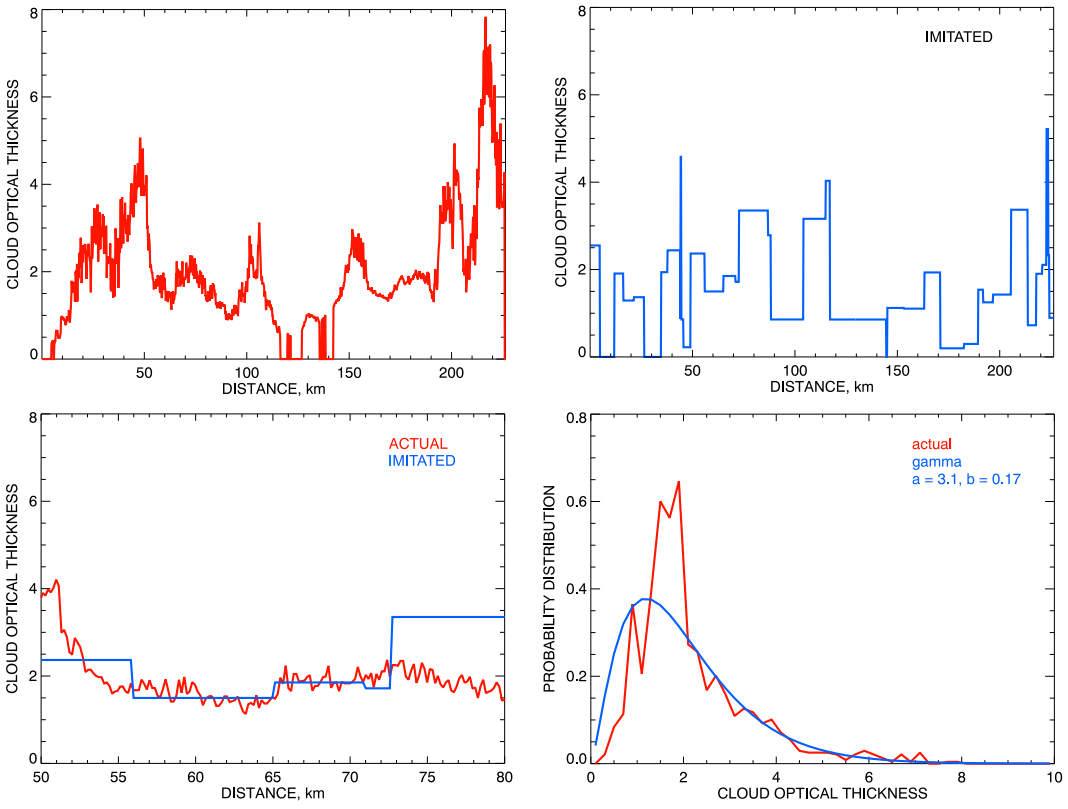

FIG. 9. As in Fig. 6, but for the altostratus (As) cloud observed by the RSP during PODEX between 1955:41 and 2014:04 UTC 1 Feb 2013.

airborne observations. They obtained the autocorrelation length estimates assuming that the autocorrelation function has exponential form [as in Eq. (72) in this paper]. Study of 2D AF allowed Schäfer et al. (2017) to characterize anisotropy of the cloud field, e.g., when clouds are elongated in the wind direction (cf. Dorff et al. 2022).

Note that at a fixed CF a decrease in L_* results in smaller clouds and smaller cloud-free areas, thus, causing extension of the total length of cloud boundaries as well as closer proximity of these boundaries to clouds interiors and exteriors. Both effects facilitate intensification of interaction between clouds and the air surrounding them. This includes entrainment of dry air and aerosol particles into the cloud causing both evaporation of cloud droplets and formation of new ones (Yang et al. 2019). On the other hand, in oceanic regions more than half of all aerosol measurements by passive satellite instruments come from near-cloud areas, where cloud-related processes may significantly modify aerosol optical depth and particle size (Várnai et al. 2017; Várnai and Marshak 2018). Cloud scale also influences the magnitude of radiative 3D effects affecting the accuracy of COT retrievals based on plane-parallel RT assumptions.

10. Concluding remarks

We introduced a parameterization of COT fields which can be potentially useful for automatic determination of cloud type in airborne and satellite observations, and also may serve as a common language connecting observations and models. This continuous-value COT model is a generalization of the binary cloud-mask model developed in the "Cellular Statistical Models of Broken Cloud Fields" series of papers which are referred to in this study as CSM1, CSM2, CSM3, and CSM4, respectively. In both models cloud fields have Markovian properties. In addition of being an "inspiration" for the COT model, its binary "ancestor" can be derived from it by setting a threshold in optical thickness to be used for separation between "cloudy" and "clear" pixels in the cloud mask (this was demonstrated in section 5 and appendix B). The parameterization of our continuous-value COT model consists of the absolute cloud fraction ν, the scale (autocorrelation) length L_*, and the COT PDF. The latter is assumed to have gamma-distribution functional shape characterized by two parameters: the effective COT τ_{eff} and the effective variance υ_{eff}.

Basing on the theoretical formulation of the model, we developed a simple algorithm for generation of synthetic COT fields with given parameters. This algorithm was successfully tested by comparison between the statistics of the generated dataset and their theoretical values computed using the model's parameters. Such statistics include the COT PDF, the structure and autocorrelation functions, as well as threshold-dependent cloud-mask characteristics (cloud fraction $\bar{c}$, scale length L_*, mean cloudy interval length $L_\bullet$, and mean clear interval length $L_\circ$).

The parameters used in our test model were derived from an LES dataset previously used in CSM2, so we in some sense tried to imitate that dataset using our statistical technique. However, the comparison between the statistics of our imitation and those of the LES dataset itself showed some discrepancies for which we currently do not have sufficient explanation. So we do not present any of such comparisons in this paper, while continue working on our model and look forward to including the LES discussion into the upcoming Part II of this series.

As one of the ways to make our model more realistic, we look for some kind of merger of the current model with that based on exponential classical Brownian random walks (which are also Markovian). The latter model of optical thickness has been introduced (in application to aerosol fields) in our previous study (Alexandrov et al. 2016b). We hope that such a merger will result in replacement of the constant COT segments in the model's realizations with those having a more realistic small-scale behavior, and also may allow for large-scale trends.

We demonstrated that the choice of the four model's parameters determines the cloud field type. To do this we took several examples of COT fields observed by the Research Scanning Polarimeter during two field campaigns, derived their parameters and "imitated" them using our statistical model. While rather simple cases of Cu, Sc, and As clouds were presented in this paper, we expect that further development of our model will allow us to describe more complex cloud systems. In particular, we anticipate using this methodology in application to the RSP data from Aerosol Cloud Meteorology Interactions Over the western Atlantic Experiment (ACTIVATE) and the upcoming Arctic Radiation-Cloud-Aerosol-Surface-Interaction Experiment (ARCSIX).

Acknowledgments. This research was funded by the NASA Radiation Sciences Program managed by Hal Maring, NASA Aerosols/Clouds/Ecosystems (ACE) project, Aerosol Cloud Meteorology Interactions Over the western Atlantic Experiment (ACTIVATE), and the Science of the *Terra*, *Aqua*, and *Suomi NPP* Program managed by Paula Bontempi.

Data availability statement. The datasets generated for or used in this study will be available from the authors upon request. All the RSP data are available from https://data.giss.nasa.gov/pub/rsp/.

APPENDIX A

Derivation of Transition Matrix from Group Properties

The binary-model transition matrix of the form Eq. (20) was derived in CSM3 in very generalized framework based on the "master matrix." Here we would like to show that the same expression can be obtained simply basing on the requirement that $\mathbf{P}(L)$ satisfies the group and limit-case properties in Eqs. (17)–(19). We will also use another simple condition, Eq. (24), following from Eqs. (18) and (19) when $L_1 = \infty$ [thus, $\mathbf{P}(L_1) = \mathbf{C}$] and $L_2 = L$:

$$\mathbf{CP}(L) = \mathbf{C}, \tag{A1}$$

where we used that $\infty + L = \infty$ on the rhs.

Let us look for $\mathbf{P}(L)$ in a very general form satisfying the row-sum condition in Eq. (8):

$$\mathbf{P}(L) = \begin{bmatrix} \xi_\bullet(L) & 1 - \xi_\bullet(L) \\ 1 - \xi_\circ(L) & \xi_\circ(L) \end{bmatrix}, \tag{A2}$$

where $\xi_\bullet(L)$ and $\xi_\circ(L)$ are independent functions of the lag and may include $\bar{c}$ and $\bar{s}$ as parameters. Without loss of generality we can use the substitutions:

$$\xi_\bullet(L) = \omega_\bullet(L) + [1 - \omega_\bullet(L)]\bar{c} = \bar{c} + \bar{s}\omega_\bullet(L) \tag{A3}$$

and

$$\xi_\circ(L) = \omega_\circ(L) + [1 - \omega_\circ(L)]\bar{s} = \bar{s} + \bar{c}\omega_\circ(L). \tag{A4}$$

In these notations

$$\mathbf{P}(L) = \begin{bmatrix} \bar{c} + \bar{s}\omega_\bullet(L) & \bar{s} - \bar{s}\omega_\bullet(L) \\ \bar{c} - \bar{c}\omega_\circ(L) & \bar{s} + \bar{c}\omega_\circ(L) \end{bmatrix}, \tag{A5}$$

which can be written as

$$\mathbf{P}(L) = \begin{pmatrix} \bar{c} & \bar{s} \\ \bar{c} & \bar{s} \end{pmatrix} + \begin{bmatrix} \bar{s}\omega_\bullet(L) & -\bar{s}\omega_\bullet(L) \\ -\bar{c}\omega_\circ(L) & \bar{c}\omega_\circ(L) \end{bmatrix}, \tag{A6}$$

or

$$\mathbf{P}(L) = \mathbf{C} + \mathbf{W}(L), \tag{A7}$$

where

$$\mathbf{W}(L) = \begin{bmatrix} \bar{s}\omega_\bullet(L) & -\bar{s}\omega_\bullet(L) \\ -\bar{c}\omega_\circ(L) & \bar{c}\omega_\circ(L) \end{bmatrix}. \tag{A8}$$

The relation in Eq. (A1) in this framework transforms into

$$\mathbf{CW}(L) = 0, \tag{A9}$$

where we used that $\mathbf{C}^2 = \mathbf{C}$. Direct matrix multiplication shows that this condition is satisfied if and only if

$$\omega_\bullet(L) \equiv \omega_\circ(L) = \omega(L). \tag{A10}$$

Thus,

$$\mathbf{W}(L) = \begin{pmatrix} \bar{s} & -\bar{s} \\ -\bar{c} & \bar{c} \end{pmatrix} \omega(L) = \mathbf{S}\omega(L), \tag{A11}$$

where

$$\mathbf{S} = \mathbf{I} - \mathbf{C}. \tag{A12}$$

Then,

$$\mathbf{P}(L) = \mathbf{C} + \mathbf{S}\omega(L). \tag{A13}$$

Note that the matrices $\mathbf{C}$ and $\mathbf{S}$ are complementary in a way similar to the relationship between $\bar{c}$ and $\bar{s}$:

$$\mathbf{C} + \mathbf{S} = \mathbf{I}. \tag{A14}$$

They also have the following properties:

$$\mathbf{C}^2 = \mathbf{C}, \quad \mathbf{CS} = \mathbf{SC} = 0, \quad \mathbf{S}^2 = \mathbf{S}, \tag{A15}$$

which transform Eq. (18) into the form

$$\mathbf{C} + \mathbf{S}\omega(L_1)\omega(L_2) = \mathbf{C} + \mathbf{S}\omega(L_1 + L_2), \tag{A16}$$

or simply

$$\omega(L_1)\omega(L_2) = \omega(L_1 + L_2). \tag{A17}$$

Equations (17) and (19) yield the conditions

$$\omega(0) = 1 \quad \text{and} \quad \omega(\infty) = 0, \tag{A18}$$

respectively. It is not difficult (while a bit lengthy) to prove that the only functional form satisfying these conditions is

$$\omega(L) = e^{-L/L_*}, \tag{A19}$$

where $L_* > 0$ is a constant. It coincides with Eq. (21) for the coefficients w_L in Eq. (20). Note also that Eq. (A13) with $\omega(L) = w_L$ is equivalent to Eq. (20).

APPENDIX B

Derivation of Cloud Mask Transition Matrix from Continuous-Value Model

The explicit expressions for the elements of the binary transition matrix $\mathbf{P}(L)$ can be derived from Eqs. (58) and (59) using convenient change of integration order:

$$\begin{aligned}
P_{\bullet\bullet}(L) &= \int_{\tau_{\rm thr}}^{\tau_{\rm max}} d\tau_1 \eta_\bullet(\tau_1) \int_{\tau_{\rm thr}}^{\tau_{\rm max}} d\tau_2 P_L(\tau_1, \tau_2) \\
P_{\bullet\circ}(L) &= \int_{\tau_{\rm thr}}^{\tau_{\rm max}} d\tau_1 \eta_\bullet(\tau_1) \int_0^{\tau_{\rm thr}} d\tau_2 P_L(\tau_1, \tau_2) \\
P_{\circ\circ}(L) &= \int_0^{\tau_{\rm thr}} d\tau_1 \eta_\circ(\tau_1) \int_0^{\tau_{\rm thr}} d\tau_2 P_L(\tau_1, \tau_2) \\
P_{\circ\bullet}(L) &= \int_0^{\tau_{\rm thr}} d\tau_1 \eta_\circ(\tau_1) \int_{\tau_{\rm thr}}^{\tau_{\rm max}} d\tau_2 P_L(\tau_1, \tau_2).
\end{aligned} \tag{B1}$$

Let us use Eq. (B1) to compute the matrix elements $P_{ij}(L)$ in the case of the continuous-value transition operator with the kernel described by Eq. (35). First, we introduce the following convenient notations:

$$\begin{aligned}
p_\bullet(\tau_1) &= \int_{\tau_{\rm thr}}^{\tau_{\rm max}} d\tau_2 P_L(\tau_1, \tau_2) \\
&= w \int_{\tau_{\rm thr}}^{\tau_{\rm max}} \delta(\tau_1 - \tau_2) d\tau_2 + w' \int_{\tau_{\rm thr}}^{\tau_{\rm max}} \rho(\tau_2) d\tau_2 \\
&= w h_\bullet(\tau_{\rm thr}, \tau_1) + w'\, \bar{c},
\end{aligned} \tag{B2}$$

where

$$h_\bullet(\tau_{\rm thr}, \tau) = \begin{cases} 1, & \tau \in [\tau_{\rm thr}, \tau_{\rm max}] \\ 0, & \tau \in [0, \tau_{\rm thr}) \end{cases} \tag{B3}$$

is a step function. Here and below we use the notations $w = w_L$ and $w' = 1 - w_L$ to make the expressions more compact. Similarly,

$$\begin{aligned}
p_\circ(\tau_1) &= \int_0^{\tau_{\rm thr}} d\tau_2 P_L(\tau_1, \tau_2) \\
&= w \int_0^{\tau_{\rm thr}} \delta(\tau_1 - \tau_2) d\tau_2 + w' \int_0^{\tau_{\rm thr}} \rho(\tau_2) d\tau_2 \\
&= w h_\circ(\tau_{\rm thr}, \tau_1) + w'\, \bar{s},
\end{aligned} \tag{B4}$$

where

$$h_\circ(\tau_{\rm thr}, \tau) = \begin{cases} 0, & \tau \in [\tau_{\rm thr}, \tau_{\rm max}] \\ 1, & \tau \in [0, \tau_{\rm thr}) \end{cases}. \tag{B5}$$

Thus, taking into account the definitions of $\eta_\bullet$ and $\eta_\circ$ and their respective normalization conditions in Eqs. (55) and (57), we can compute the transition probabilities in Eq. (B1):

$$\begin{aligned}
P_{\bullet\bullet}(L) &= \int_{\tau_{\rm thr}}^{\tau_{\rm max}} d\tau_1 \eta_\bullet(\tau_1) p_\bullet(\tau_1) = w + w'\, \bar{c} \\
P_{\bullet\circ}(L) &= \int_{\tau_{\rm thr}}^{\tau_{\rm max}} d\tau_1 \eta_\bullet(\tau_1) p_\circ(\tau_1) = w'\, \bar{s} \\
P_{\circ\circ}(L) &= \int_0^{\tau_{\rm thr}} d\tau_1 \eta_\circ(\tau_1) p_\circ(\tau_1) = w + w'\, \bar{s} \\
P_{\circ\bullet}(L) &= \int_0^{\tau_{\rm thr}} d\tau_1 \eta_\circ(\tau_1) p_\bullet(\tau_1) = w'\, \bar{c}.
\end{aligned} \tag{B6}$$

And the whole binary transition matrix, Eq. (7), can be written as

$$\mathbf{P}(L) = \begin{bmatrix} w_L + (1 - w_L)\bar{c} & (1 - w_L)\bar{s} \\ (1 - w_L)\bar{c} & w_L + (1 - w_L)\bar{s} \end{bmatrix}, \tag{B7}$$

or equivalently

$$\mathbf{P}(L) = w_L \begin{pmatrix} 1 & 0 \\ 0 & 1 \end{pmatrix} + (1 - w_L) \begin{pmatrix} \bar{c} & \bar{s} \\ \bar{c} & \bar{s} \end{pmatrix}, \tag{B8}$$

which coincides with Eq. (20) if we use the notation Eq. (16) for the matrix $\mathbf{C}$.

REFERENCES

Ackerman, A. S., M. P. Kirkpatrick, D. E. Stevens, and O. B. Toon, 2004: The impact of humidity above stratiform clouds on indirect aerosol climate forcing. *Nature*, **432**, 1014–1017, https://doi.org/10.1038/nature03174.

Alexandrov, M. D., and A. Marshak, 2017: Cellular statistical models of broken cloud fields. Part III: Markovian properties.

J. Atmos. Sci., **74**, 2921–2935, https://doi.org/10.1175/JAS-D-17-0075.1.

——, and ——, 2019: Cellular statistical models of broken cloud fields. Part IV: Effects of pixel size on idealized satellite observations. *J. Atmos. Sci.*, **76**, 1329–1348, https://doi.org/10.1175/JAS-D-18-0345.1.

——, ——, B. Cairns, A. A. Lacis, and B. E. Carlson, 2004: Scaling properties of aerosol optical thickness retrieved from ground-based measurements. *J. Atmos. Sci.*, **61**, 1024–1039, https://doi.org/10.1175/1520-0469(2004)061<1024:SPOAOT>2.0.CO;2.

——, ——, and A. S. Ackerman, 2010a: Cellular statistical models of broken cloud fields. Part I: Theory. *J. Atmos. Sci.*, **67**, 2125–2151, https://doi.org/10.1175/2010JAS3364.1.

——, A. S. Ackerman, and A. Marshak, 2010b: Cellular statistical models of broken cloud fields. Part II: Comparison with a dynamical model and statistics of diverse ensembles. *J. Atmos. Sci.*, **67**, 2152–2170, https://doi.org/10.1175/2010JAS3365.1.

——, B. Cairns, C. Emde, A. S. Ackerman, and B. van Diedenhoven, 2012: Accuracy assessments of cloud droplet size retrievals from polarized reflectance measurements by the Research Scanning Polarimeter. *Remote Sens. Environ.*, **125**, 92–111, https://doi.org/10.1016/j.rse.2012.07.012.

——, and Coauthors, 2015: Liquid water cloud properties during the Polarimeter Definition Experiment (PODEX). *Remote Sens. Environ.*, **169**, 20–36, https://doi.org/10.1016/j.rse.2015.07.029.

——, B. Cairns, C. Emde, A. S. Ackerman, M. Ottaviani, and A. P. Wasilewski, 2016a: Derivation of cumulus cloud dimensions and shape from the airborne measurements by the Research Scanning Polarimeter. *Remote Sens. Environ.*, **177**, 144–152, https://doi.org/10.1016/j.rse.2016.02.032.

——, I. V. Geogdzhayev, K. Tsigaridis, A. Marshak, R. C. Levy, and B. Cairns, 2016b: New statistical model for variability of aerosol optical thickness: Theory and application to MODIS data over ocean. *J. Atmos. Sci.*, **73**, 821–837, https://doi.org/10.1175/JAS-D-15-0130.1.

——, and Coauthors, 2016c: Polarized view of supercooled liquid water clouds. *Remote Sens. Environ.*, **181**, 96–110, https://doi.org/10.1016/j.rse.2016.04.002.

——, and Coauthors, 2018: Retrievals of cloud droplet size from the research scanning polarimeter data: Validation using in situ measurements. *Remote Sens. Environ.*, **210**, 76–95, https://doi.org/10.1016/j.rse.2018.03.005.

Astin, I., and B. G. Latter, 1998: A case for exponential cloud fields? *J. Appl. Meteor.*, **37**, 1375–1382, https://doi.org/10.1175/1520-0450(1998)037<1375:ACFECF>2.0.CO;2.

Barker, H. W., 1996: A parameterization for computing grid-averaged solar fluxes for inhomogeneous marine boundary layer clouds. Part I: Methodology and homogeneous biases. *J. Atmos. Sci.*, **53**, 2289–2303, https://doi.org/10.1175/1520-0469(1996)053<2289:APFCGA>2.0.CO;2.

——, B. A. Weilicki, and L. Parker, 1996: A parameterization for computing grid-averaged solar fluxes for inhomogeneous marine boundary layer clouds. Part II: Validation using satellite data. *J. Atmos. Sci.*, **53**, 2304–2316, https://doi.org/10.1175/1520-0469(1996)053<2304:APFCGA>2.0.CO;2.

Berg, L. K., and E. I. Kassianov, 2008: Temporal variability of fair-weather cumulus statistics at the ACRF SGP site. *J. Climate*, **21**, 3344–3358, https://doi.org/10.1175/2007JCLI2266.1.

Cahalan, R. F., 1994: Bounded cascade clouds: Albedo and effective thickness. *Nonlinear Processes Geophys.*, **1**, 156–167, https://doi.org/10.5194/npg-1-156-1994.

——, and J. H. Joseph, 1989: Fractal statistics of cloud fields. *Mon. Wea. Rev.*, **117**, 261–272, https://doi.org/10.1175/1520-0493(1989)117<0261:FSOCF>2.0.CO;2.

Davis, A., A. Marshak, W. Wiscombe, and R. Cahalan, 1994: Multifractal characterizations of nonstationarity and intermittency in geophysical fields: Observed, retrieved, or simulated. *J. Geophys. Res.*, **99**, 8055–8072, https://doi.org/10.1029/94JD00219.

Dorff, H., H. Konow, and F. Ament, 2022: Horizontal geometry of trade wind cumuli—Aircraft observations from a shortwave infrared imager versus a radar profiler. *Atmos. Meas. Tech.*, **15**, 3641–3661, https://doi.org/10.5194/amt-15-3641-2022.

Hansen, J. E., and L. D. Travis, 1974: Light scattering in planetary atmospheres. *Space Sci. Rev.*, **16**, 527–610, https://doi.org/10.1007/BF00168069.

Ibe, O., 2013: *Markov Processes for Stochastic Modeling.* 2nd ed. Elsevier, 515 pp.

Joseph, J. H., and R. F. Cahalan, 1990: Nearest neighbor spacing of fair weather cumulus clouds. *J. Appl. Meteor. Climatol.*, **29**, 793–805, https://doi.org/10.1175/1520-0450(1990)029<0793:NNSOFW>2.0.CO;2.

Kassianov, E., 2003: Stochastic radiative transfer in multilayer broken clouds. Part I: Markovian approach. *J. Quant. Spectrosc. Radiat. Transfer*, **77**, 373–393, https://doi.org/10.1016/S0022-4073(02)00170-X.

——, and D. Veron, 2011: Stochastic radiative transfer in Markovian mixtures: Past, present, and future. *J. Quant. Spectrosc. Radiat. Transfer*, **112**, 566–576, https://doi.org/10.1016/j.jqsrt.2010.06.011.

King, M. D., S. Platnick, W. P. Menzel, S. A. Ackerman, and P. A. Hubank, 2013: Spatial and temporal distribution of clouds observed by MODIS onboard the Terra and Aqua satellites. *IEEE Trans. Geosci. Remote Sens.*, **51**, 3826–3852, https://doi.org/10.1109/TGRS.2012.2227333.

Koren, I., L. Oreopoulos, G. Feingold, L. A. Remer, and O. Altaratz, 2008: How small is a small cloud? *Atmos. Chem. Phys.*, **8**, 3855–3864, https://doi.org/10.5194/acp-8-3855-2008.

Kulkarni, V. G., 2011: *Introduction to Modeling and Analysis of Stochastic Systems*. 2nd ed. Springer, 326 pp.

Lane, D. E., K. Goris, and R. C. J. Somerville, 2002: Radiative transfer through broken clouds: Observations and model validation. *J. Climate*, **15**, 2921–2933, https://doi.org/10.1175/1520-0442(2002)015<2921:RTTBCO>2.0.CO;2.

Levermore, C. D., J. Wong, and G. C. Pomraning, 1988: Renewal theory for transport processes in binary statistical mixtures. *J. Math. Phys.*, **29**, 995–1004, https://doi.org/10.1063/1.527997.

Lovejoy, S., and D. Schertzer, 2012: Haar wavelets, fluctuations and structure functions: Convenient choices for geophysics. *Nonlinear Processes Geophys.*, **19**, 513–527, https://doi.org/10.5194/npg-19-513-2012.

Marshak, A., A. Davis, R. F. Cahalan, and W. J. Wiscombe, 1993: Multi-singular and multi-affine properties of bounded cascade models. *Fractals*, **1**, 702–710, https://doi.org/10.1142/S0218348X93000733.

——, ——, ——, and ——, 1994: Bounded cascade models as non-stationary multifractals. *Phys. Rev.*, **49**, 55–69, https://doi.org/10.1103/PhysRevE.49.55.

Meneveau, C., and K. R. Sreenivasan, 1987: Simple multifractal cascade model for fully developed turbulence. *Phys. Rev. Lett.*, **59**, 1424–1427, https://doi.org/10.1103/PhysRevLett.59.1424.

Morf, H., 1998: The stochastic two-state solar irradiance model (STSIM). *Sol. Energy*, **62**, 101–112, https://doi.org/10.1016/S0038-092X(98)00004-8.

——, 2011: The stochastic two-state cloud cover model STSCCM. *Sol. Energy*, **85**, 985–999, https://doi.org/10.1016/j.solener.2011.02.015.

Morrison, H., and A. Gettelman, 2008: A new two-moment bulk stratiform cloud microphysics scheme in the Community Atmosphere Model, version 3 (CAM3). Part I: Description and numerical tests. *J. Climate*, **21**, 3642–3659, https://doi.org/10.1175/2008JCLI2105.1.

Nakajima, T., and M. D. King, 1990: Determination of the optical thickness and effective particle radius of clouds from reflected solar radiation measurements. Part I: Theory. *J. Atmos. Sci.*, **47**, 1878–1893, https://doi.org/10.1175/1520-0469(1990)047<1878:DOTOTA>2.0.CO;2.

Pincus, R., S. A. McFarlane, and S. A. Klein, 1999: Albedo bias and the horizontal variability of clouds in subtropical marine boundary layers: Observations from ships and satellite. *J. Geophys. Res.*, **104**, 6183–6191, https://doi.org/10.1029/1998JD200125.

Plank, V. G., 1969: The size distribution of cumulus clouds in representative Florida populations. *J. Appl. Meteor.*, **8**, 46–67, https://doi.org/10.1175/1520-0450(1969)008<0046:TSDOCC>2.0.CO;2.

Pomraning, G. C., 1989: Statistics, renewal theory and particle transport. *J. Quant. Spectrosc. Radiat. Transfer*, **42**, 279–293, https://doi.org/10.1016/0022-4073(89)90074-5.

Rodts, S. M. A., P. G. Duynkerke, and H. J. J. Jonker, 2003: Size distributions and dynamical properties of shallow cumulus clouds from aircraft observations and satellite data. *J. Atmos. Sci.*, **60**, 1895–1912, https://doi.org/10.1175/1520-0469(2003)060<1895:SDADPO>2.0.CO;2.

Schäfer, M., E. Bierwirth, A. Ehrlich, E. Jäkel, F. Werner, and M. Wendisch, 2017: Directional, horizontal inhomogeneities of cloud optical thickness fields retrieved from ground-based and airborne spectral imaging. *Atmos. Chem. Phys.*, **17**, 2359–2372, https://doi.org/10.5194/acp-17-2359-2017.

Schertzer, D., and S. Lovejoy, 1987: Physical modeling and analysis of rain clouds by anisotropic scaling multiplicative processes. *J. Geophys. Res.*, **92**, 9693–9714, https://doi.org/10.1029/JD092iD08p09693.

Seelig, T., H. Deneke, J. Quaas, and M. Tesche, 2021: Life cycle of shallow marine cumulus clouds from geostationary satellite observations. *J. Geophys. Res. Atmos.*, **126**, e2021JD035577, https://doi.org/10.1029/2021JD035577.

Sinclair, K., B. van Diedenhoven, B. Cairns, J. Yorks, A. Wasilewski, and M. McGill, 2017: Remote sensing of multiple cloud layer heights using multi-angular measurements. *Atmos. Meas. Tech.*, **10**, 2361–2375, https://doi.org/10.5194/amt-10-2361-2017.

——, ——, ——, M. Alexandrov, R. Moore, E. Crosbie, and L. Ziemba, 2019: Polarimetric retrievals of cloud droplet number concentrations. *Remote Sens. Environ.*, **228**, 227–240, https://doi.org/10.1016/j.rse.2019.04.008.

Stevens, B., and Coauthors, 2001: Simulations of trade wind cumuli under a strong inversion. *J. Atmos. Sci.*, **58**, 1870–1891, https://doi.org/10.1175/1520-0469(2001)058<1870:SOTWCU>2.0.CO;2.

Várnai, T., and A. Marshak, 2018: Satellite observations of cloud-related variations in aerosol properties. *Atmosphere*, **9**, 430, https://doi.org/10.3390/atmos9110430.

——, ——, and T. F. Eck, 2017: Observation-based study on aerosol optical depth and particle size in partly cloudy regions. *J. Geophys. Res. Atmos.*, **122**, 10 013–10 024, https://doi.org/10.1002/2017JD027028.

Vogelmann, A. M., and Coauthors, 2012: RACORO extended-term aircraft observations of boundary layer clouds. *Bull. Amer. Meteor. Soc.*, **93**, 861–878, https://doi.org/10.1175/BAMS-D-11-00189.1.

Wielicki, B. A., and R. M. Welch, 1986: Cumulus cloud properties derived using Landsat satellite data. *J. Appl. Meteor. Climatol.*, **25**, 261–276, https://doi.org/10.1175/1520-0450(1986)025<0261:CCPDUL>2.0.CO;2.

Wood, R., and P. R. Field, 2011: The distribution of cloud horizontal sizes. *J. Climate*, **24**, 4800–4816, https://doi.org/10.1175/2011JCLI4056.1.

Yang, W., A. Marshak, and G. Wen, 2019: Cloud edge properties measured by the ARM shortwave spectrometer over ocean and land. *J. Geophys. Res. Atmos.*, **124**, 8707–8721, https://doi.org/10.1029/2019JD030622.